Preprint

GelCam: Visualizing Episodic Sinking Particle Flux via a Polyacrylamide Gel-Based Sediment Trap

Yixuan Song[*1], Melissa Omand[1], Colleen A. Durkin[2], Margaret L. Estapa[3], and Ken O. Buesseler[4]

[1]Graduate School of Oceanography, University of Rhode Island, Narragansett, RI, USA

[2]Monterey Bay Aquarium Research Institute, Moss Landing, CA, USA

[3]School of Marine Sciences, Darling Marine Center, University of Maine, Walpole, ME, USA

[4]Woods Hole Oceanographic Institution, Woods Hole, MA, USA

[*]Corresponding author: Yixuan Song, yixuan.song@uri.edu

GelCam: Visualizing Episodic Sinking Particle Flux via a Polyacrylamide Gel-Based Sediment Trap

Yixuan Song*[1], Melissa Omand[1], Colleen A. Durkin[2], Margaret L. Estapa[3], and Ken O. Buesseler[4]

[1]Graduate School of Oceanography, University of Rhode Island, Narragansett, RI, USA

[2]Monterey Bay Aquarium Research Institute, Moss Landing, CA, USA

[3]School of Marine Sciences, Darling Marine Center, University of Maine, Walpole, ME, USA

[4]Woods Hole Oceanographic Institution, Woods Hole, MA, USA

*Corresponding author: Yixuan Song, yixuan.song@uri.edu

Running Head: GelCam: Visualizing Episodic Particle Flux

Keywords: Biological carbon pump, sediment traps, marine snow, fecal pellets, aggregates, particles

ABSTRACT

While particle-intercepting traps remain a dominant method for quantifying the contribution of sinking particles to the biological carbon pump, fluxes are typically integrated over days to months. Observations of time-varying particle flux over shorter durations are very limited. To this end, we prototyped a camera system called “GelCam” which captures a rapid time-lapse image sequence of particles that settle into a polyacrylamide gel layer located at the base of a sediment trap tube. Here, we describe the system design, post image processing, and results from nine deployments during the EXPORTS campaigns in 2018 and 2021 in the North Pacific and Atlantic ocean. Because wave-driven oscillations of the surface-tethered traps produced a lateral motion of the settled particles, we applied a cross-correlation method for tracking individual particles over time. All particles were subsequently classified into one of six categories based on visual traits, and then quantified into a particulate organic carbon (POC) flux. Using this image-based approach, we are able to distinguish differences in depth-based transfer efficiency among groups, and detect a diel variation in fecal pellet flux. Additionally, the GelCam resolved flux events on timescales shorter than days, allowing for the investigation of covariance among different particle types over short timescales. Paired with the direct recovery of samples to quantify carbon content and high resolution particle images, this approach will enhance our ability to resolve sinking “events” that occur episodically and may be missed when integrating over a traditional trap deployment.

INTRODUCTION

The ocean sink provides a net uptake of approximately $2.8 \cdot 10^{15}$ g of carbon annually, which accounts for more than 25% of anthropogenic CO_2 emissions (Friedlingstein et al., 2023). Among processes of marine carbon sequestration, sinking particles transport $\sim 10^{15}$ g/yr of carbon from the surface ocean to the deep ocean (Middelburg, 2011; Muller-Karger, 2005; Henson et al., 2011). Knowing the biological carbon pump is critical for predicting climate change effects. There are a few challenges to overcome before we can accurately model the ocean carbon uptake process. First, the carbon transport is driven by complex biophysical and chemical processes (Nowicki et al., 2022). Photosynthesis by phytoplankton (Basu and Mackey, 2018), consumption and production by zooplankton and fish (Cavan et al., 2017), and sinking of marine particles (De La Rocha and Passow, 2007) contribute to the high uncertainty in modeling the carbon transport. Additionally, aggregation (Burd and Jackson, 2009; Alldredge and Gotschalk, 1988), disaggregation (Briggs et al., 2020; Song et al., 2023), and microbial degradation occurring on particles (Collins et al., 2015), alter the particle size and contribute to the high variability in the sinking velocity of marine particles (McDonnell and Buesseler, 2010). Moreover, spatial and temporal variability further complicates the modeling of global biogeochemical cycles (Piao et al., 2013; SierraI et al., 2007). These challenges along with observational limitations in remote areas and deep sea environments, substantially constrains our understanding of carbon flux within the ocean.

Sediment traps provide a direct measurement of sinking marine particles, as the downward carbon flux can be retrieved from the total organic matter captured over a period of time within a fixed collection area of a tube or a funnel (Buesseler et al., 2007). Traditional sediment trap measurements provide an integrated carbon flux sample collected over time scales ranging from days to months (Buesseler et al., 2007). Post analyses are necessary for most traditional sediment trap measurements. For example, Muller and Suess (1979) applied elemental combustion analysis to measure the organic carbon content in sediment trap samples. Durkin et al. (2021) used microscopic imaging techniques to analyze particles preserved in the polyacrylamide gel. In addition to being labor-demanding, the traditional sediment trap method is limited in its ability to assess episodic variations on timescales of hours.

Classifying sinking particle types is important for accurately predicting the carbon flux because each particle type contributes to carbon transport in its unique way. For example, zooplankton fecal pellets have been observed to play a major role in controlling carbon flux in some studies (e.g., (Cavan et al., 2015; Turner, 2002)). More specifically, Durkin et al. (2021) and Steinberg et al. (2023) emphasized the role of salp fecal pellets in the Subarctic Northeast Pacific Ocean. Additionally, the importance of large marine snow particles is highlighted in other studies, by which aggregation enhances the transport of organic matter (Alldredge and Silver, 1988; Fowler and Knauer, 1986). Contributions of phytoplankton (Durkin et al., 2016), mini fecal pellets (Gowing and Silver, 1985), and physical subduction (Omand et al., 2015) that includes particles cannot be ignored as well. However, the composition of sinking particle flux varies in space and time, leading to challenges in their classification. Developing a time-resolved particle classification system for sediment trap samples is needed. Using an imaging system, such as optical sediment traps, not only simplifies sample processing but enables the evaluation of flux components across different particle types.

To better understand and constrain temporal variability in particle fluxes and identify the ecological sources that drive these variations, we have developed a novel, low-cost, and easy-to-deploy instrument, named “GelCam”. This instrument allows for a rapid evaluation without extensive post analysis, and chronological diagnosis of particle identities. Here we demonstrate the GelCam design and analyze episodic particulate organic carbon fluxes from ten datasets collected from two NASA EXPORTS (EXport Processes in the Ocean from Remote Sensing) field campaigns. The image post-processing contains a particle tracking algorithm and particle classification, which provides the arrival time and morphology of each particle. The GelCam with the framework of imaging processing can be applied to quantify the particle flux using two methods, with one based on cumulative particle areas and the other one based on the particle tracking and classification results. Here we model the particulate organic carbon from particle images and compare the fluxes between GelCam and other methods. We also present the diel changes of fecal pellet fluxes and investigate flux events attributable to different particle types. We finally discuss the benefits of using the GelCam to extract quantitative carbon flux and facilitate modeling of the biological carbon pump.

MATERIALS AND PROCEDURES

GelCam design

The GelCam is a time-lapse camera system designed to pair with a particle-intercepting sediment trap and it has two iterations that have already been deployed. In the current design, we used a cylindrical trap with an outer diameter of 127 mm, and a total length of 700 mm (Figure 1 (A)). A lid closure method used a bungee that was mounted to either a horizontal bar or to the side wall of the tube (since 2021). The open bottom of the tube was attached to the camera system with opposed flanges and an o-ring face seal. Before sealing the camera to the tube, a shallow container with a transparent bottom was filled with a ~10 mm thick layer of polyacrylamide gel and placed at the base of the trap, and served to retain deposited particles.

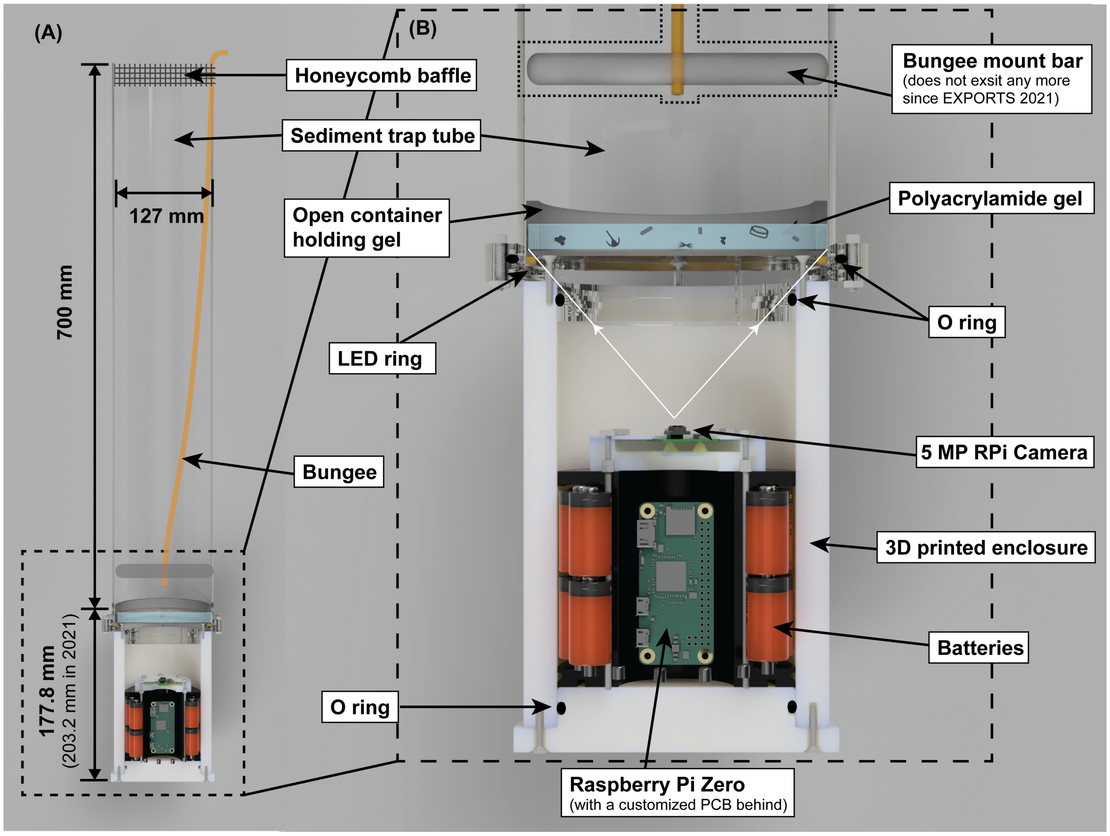

Figure 1. Schematic diagram of the GelCam system: (A) overview of the sediment trap with the GelCam attached to the bottom, and (B) detailed cross-section view within the enclosure.

The GelCam housing was composed of an optically clear one inch thick acrylic top lid, a cylindrical acetal resin (Delrin) tube and a acetal resin bottom lid (Figure 1(A)). The housing length was 177.8 mm during EXPORTS 2018. An upgrade in 2021 increased the length to 203.2 mm to provide more inner space and a larger field of view (FOV). The top lid contained a potted LED ring with a width of 4 mm and an outer diameter of 120 mm using clear epoxy resin, located on the upper surface to eliminate direct light or reflections and allowing only diffuse, scattered light to enter the camera. Brackets fabricated by 3D printing techniques and designed to secure the batteries and electronics, were integrated within the housing. We used 7 packs of 12 V (nominal) stacks, each consisting of 4 CR123A batteries, yielding 134 Watt-hrs. The batteries were used to power a Arduino Nano micro controller, a Raspberry Pi Zero WiFi single-board computer, a Raspberry Pi camera module, and the LED ring. The low-power Arduino was used to duty cycle the R-Pi Zero, enabling us the sustain weeks-long deployments with photos every 20 minutes. The camera was mounted facing upwards toward the gel container with a viewing axis aligned with the central axis of the sediment trap, enabling us to image nearly the entire base of the gel-filled cup.

The camera module had a sensor resolution of 2592 × 1944 pixels. The lens used in the 2018 expedition provided a FOV of approximately 55.2 mm × 41.4 mm which translated to a pixel resolution of 21.3 μm per pixel. The taller housing used since 2021 expanded the FOV but provided a smaller pixel resolution of 25.5 μm per pixel. We calibrated the cameras before each deployment, with an optical depth trained on the deepest layer of the gel where the particles accumulated. The Arduino Nano was programmed to duty cycle the R-Pi at 20 minute intervals. However due to uncertainties in the timer built into the ATMEGA328P micro controller, the actual time interval varied by deployments within a few minutes. Fortunately, we also integrated a highly accurate real time clock, which logged the time stamp for each image. Later versions of this system have replaced the Arduino-based micro controller for a more accurate and lower power option. Images were archived on a 64GB SD card within the R-Pi Zero. This configuration had sufficient power to take photos at 20 minute intervals for 8 days. The operational depth rating of the housing was 300m.

Cruises and sampling platform

Gelcams were deployed in the subarctic North Pacific (NP) and North Atlantic (NA) during two EXPORTS cruises. The former cruise conducted three deployments aboard the *R/V Roger Revelle* near Ocean Station Papa (50°N, 145°W) during three repeating sampling cycles identified as Deployment 1, 2, and 3, from August 15 to September 5 2018 (Table 1) (other NASA EXPORTS papers referred the deployment duration as "epoch"). The deployment plan is presented by Siegel et al. (2021) and sediment trap details are presented by Estapa et al. (2021). On a surface-tethered trap (STT) array, we installed the GelCam at three near-surface traps, corresponding to 95, 145, and 195 m in Deployment 1. Weather-induced damage required subsequent repairs, causing a 10 m increase in depth during Deployment 2 and 3. The second EXPORTS campaign conducted measurements on the *R/V James Cook* on May 5-8, 2021 near the Porcupine Abyssal Plain Sustained Observatory site (49°N, 16°W). Durkin et al. (2021) described the preparation of the sediment trap tube and polyacrylamide gel in detail.

During EXPORTS NP, all GelCam cameras were functional, at all three depths across three deployment durations, obtaining 9 total records. GelCams deployed during Deployment 1 and 3 collected more than 400 images each within more than six days of deployments. Gelcams during Deployment 2 recorded about 360 images. During EXPORTS NA, housing failures resulted in only one successful record collected at 125 m depth. This measurement recorded 169 images within four days. Additionally, the camera system infrequently encountered a compression issue while transmitting the data to the SD card, leading to anomalous images being saved. These corrupted image files could not be used for any image processing. A manual check identified 25 images with quality issues out of 3,846.

Table 1. Summary of sampling locations. *The North Atlantic deployment applied a hardware upgrade of a larger FOV and eliminated the bungee mount bar.

Deployment	Cruise	Location	Dates	Depths	# of images
NP Deployment 1 STT 1, 2, 3	R/V Revelle	Subarctic North Pacific 50.1°N, 145.1°W	Aug. 15-21 2018 Deployment 1	95 m 145 m 195 m	445 410 443
NP Deployment 2 STT 1, 2, 3	R/V Revelle	Subarctic North Pacific 50.4°N, 145.1°W	Aug. 24-28 2018 Deployment 2	105 m 155 m 205 m	369 368 341
NP Deployment 3 STT 1, 2, 3	R/V Revelle	Subarctic North Pacific 50.6°N, 144.9°W	Aug. 31-Sep. 5 2018 Deployment 3	105 m 155 m 205 m	442 446 413
NA Deployment	R/V James Cook	Subarctic North Atlantic 48.9°N, 15.0°W	May 5-8 2021	125 m	169*

Imaging processing procedures

Color decomposition to remove ambient light variations

An image processing pipeline was developed for the GelCam images. Each raw image (see example in Figure 2(A)) shows the LED near the outer edge of the gel cup (large white circle), the bar holding the bungee (EXPORTS 2018 only), and darkened areas of the background where the clear tube was mounted to the STT frame and near the top at the lid attachment. Here we created a static mask to exclude the LED ring, the bungee mount bar, and other bright background objects from the FOV. Areas of very bright pixels represented the LED ring near the edge and the orange bungee in the middle. At the same time, less bright areas of the bungee mount bar were outlined and then masked out by two fitted straight lines. During daytime, ambient sunlight caused portions of the background to appear in a green-blue hue, even at depths up to 205 m. By decomposing the images into the green, blue, and red channel (Figure 2(B) and (C)), we found that the red channel was highly effective at filtering out the ambient light, since at the depth of the traps, all of the ambient red wavelengths have been absorbed by seawater. We then converted the red channel image to a gray scale for region of interest (ROI) identification.

The temporal variations in the blue and green channel were very effective at illustrating the day-and-night cycle in ambient sunlight. Since we were interested in diurnal variation of particle flux, it was crucial that we account for any variations in particle detection likelihood or contouring that might arise due to the variations of background light. As particles occupied less than 7.5% of the field of view, the blue and green pixel intensity (averaged over each image) provided a reliable representation of the overall ambient light changes over time (Figure 3). The variations were very low during nighttime, while noticeable peaks were observable around mid-day. A strong correlation was found between the lighting variations within the green and blue channels and concurrent measurements of surface light levels obtained from a Photosynthetically Active Radiation (PAR) sensor deployed on a WireWalker (Suppl. Mat., Figure S3). The example sequence of a single particle over time shown in Figure 3 highlights the RGB color variations between night and day, with the background color turning green during the daylight hours. The day-night pattern was not evident in the normalized red channel, and so by using only the red channel for particle edge detection, we markedly reduced the sensitivity to background light variations. Selection of the red channel also had the effect of eliminating the color variation associated with the trap tube components that were far away from the illumination source, such as the tube bracket and top lip (see the darker concentric rings in Figure 2(A) compared to (C)).

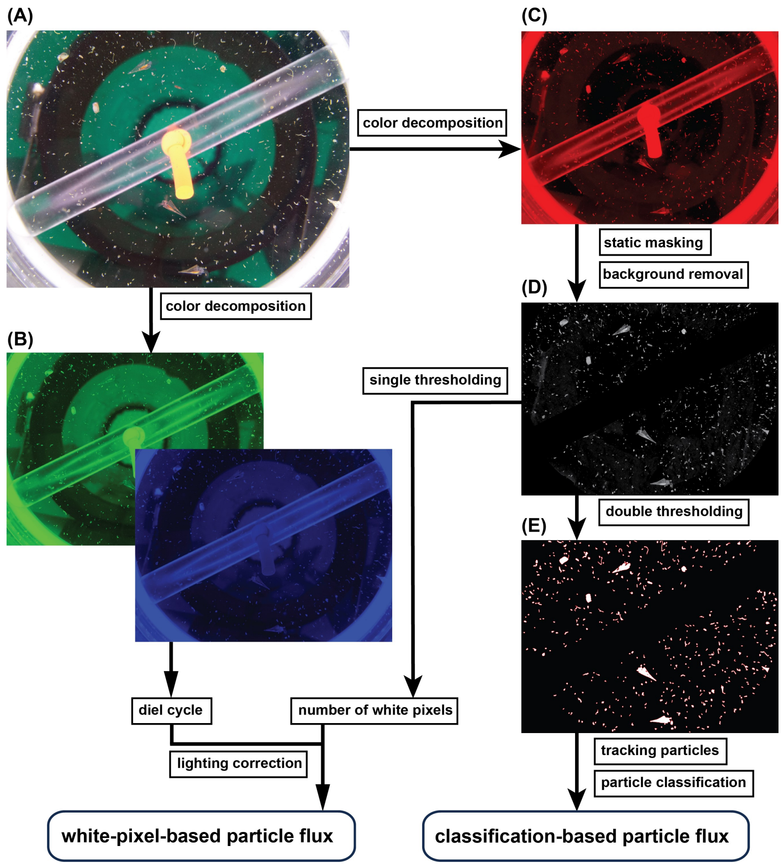

Figure 2. Pipeline of image pre-processing procedures, with (A) original captured image, (B) decomposed images in green and blue channels, (C) red channel image, (D) masked grayscale image after background removal, and (E) binarized image with particles outlined. The semitransparent mount bar with the orange bungee did not exist during EXPORTS 2021.

Background removal

The next step in image preparation was masking of the static parts of the image that contained strongly contrasting tube parts close to the illumination source, such as the bungee bar and knot (Figure 2(C)). Here we used a proper orthogonal decomposition (POD) method, which has been proven effective in particle image velocimetry (PIV) (Mendez et al., 2017) and particle tracking

(Song and Rau, 2022). In our current configuration, we observed particle movements and rotations driven by local circulations and small-scale flows acting on the sediment trap. Such movements made the application of POD-based background removal possible. We implemented this by applying a static mask first to all images in the red channel, followed by a singular value decomposition. Subsequently, we eliminated the first principal component and reconstructed the image frames. Figure 2 (D) shows the resulting background-removed product of the masked red-channel image in (C). Using this method, particles were successfully preserved while the background was eliminated.

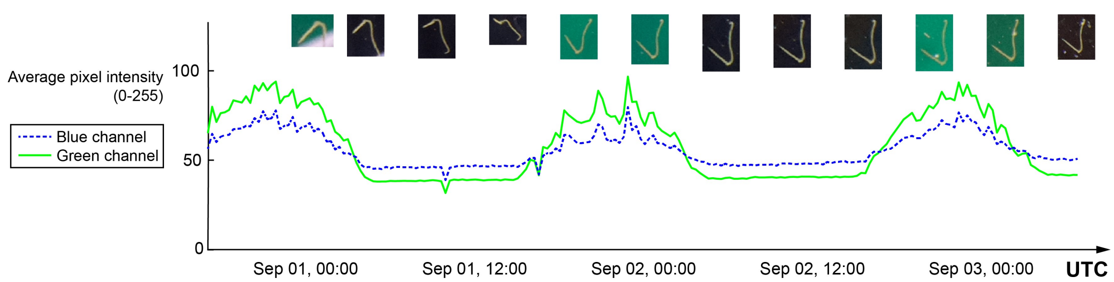

Figure 3. Example day-and-night cycle represented by the average pixel intensities in green (solid line) and blue (dotted line) channels, combined with one example tracking series at a time interval of roughly 6 hours (16 frames) during Deployment 3 STT 1. See Figure S3 in supplement materials for correlations with PAR signals.

Particle contouring

Next we developed a double-threshold method to convert particles in the grayscale image to binary form. First, we computed the Otsu threshold (Otsu, 1979) for each image frame after the background removal. We then averaged these thresholds to establish a global black-and-white cutoff. The first round of binarization was mostly effective, but we found that using a global threshold did not completely outline particles with looser structures, such as aggregates, which had segmented shapes. To remedy this, we set an additional but lower threshold by subtracting three standard deviations of the pixel intensities from the global threshold. The lower cut-off value retained relatively dimmer pixels, often bridging between aggregate segments, although it also included some background noise. Here we retained pixels that passed the lower threshold if they connected with pixels that had passed the first global threshold. Lastly, we applied an area filter with a 50 pixels minimum (*ESD* (equivalent spherical diameter) ~ 170 μm), to exclude noise features and small particles that lacked sufficient morphological details for classification. We compiled a table assigning each particle a unique index and summarizing the images and morphology of particles in all image frames. Figure 2 (E) shows an example of the particles that passed our binarization method, outlined in red.

Particle tracking

We implemented a particle tracking method to continuously monitor the particle motion within the gel and measure the particle flux. The surface tethered sediment trap experienced fairly strong vertical and rotational wave-driven motions during deployment. For the first two deployments in the North Pacific, the gel cup was freely able to rotate within the tube, and this appeared to enhance the rotational movements of the gel. Thus, the particles experienced horizontal motion relative to the camera throughout the deployments (See supplementary videos). The high viscosity of the gel helped to keep these motions fairly smooth, with strong auto-correlation between the particle motions that were fairly straightforward to track by eye and with our bulk motion routines. We first utilized particle image velocimetry (PIV) to capture the bulk movement between two consecutive image frames. We used the open-source PIVlab code (Thielicke and

Stamhuis, 2014) to implement a single PIV pass to detect the velocities associated with the bulk motion. A square evaluation window with a size of 320 × 320 ($x \times y$) pixels was selected based on the maximum distant particles seemed to travel within the 20 min image interval. This window size also ensured sufficient bright pixels for cross correlation in the first few frames. We set the window overlap at 50% in both x and y directions. Following this, a two-dimensional Gaussian regression model (Nobach and Honkanen, 2005) provided a sub-pixel estimation. Additionally, we applied a universal outlier detection after the single pass to eliminate inaccurate vectors (Westerweel and Scarano, 2005). The PIV analysis yielded a bulk velocity field of 15 × 11 vectors. To approximate particle movement between frames, we applied a two-dimensional interpolation method to each particle's centroid position.

Next, we performed another cross-correlation method to precisely track each particle's movement between adjacent frames. Here we created two interrogation windows, w_1 and w_2, from two successive frames. We defined the first interrogation window, w_1, as a rectangular box around a particle indexed i after the contouring. Each side of the window had a minimum distance of 8 pixels from the particle's edge. The second interrogation window, w_2 in the following frame, was centered on the guessed position, based on the particle's estimated centroid after interpolating the PIV vectors. We expanded this window size by 16 pixels for large particles (if the longest particle dimension was greater than 16 pixels), and by 8 pixels if the particle was small (less than 16 pixels). We then conducted a cross correlation search within w_2 to find the best match. The location that generated the best correlation, with a correlation coefficient > 0.7 and a distinct peak in the correlation plane, was allocated as position i' in the next frame. If this location matched a particle j in the second frame ($j = i'$), we linked the two particle indices i and j in our tracking series. Conversely, we considered particles without matches as new arrivals. Particle images in

Figure 3 illustrate one tracking example of a long fecal pellet that applied this algorithm. Despite challenges including translation, deformation, re-orientation, and background lighting variations, our method effectively identified the same particles over consecutive images. To verify, we randomly selected and manually examined 500 particle sequences (out of 43,286 total).

In some cases, two particles overlapped and crossed each other (28% of the total). The overlap issue became increasingly problematic in the later deployment stage as more particles appeared in the FOV. In these cases, we flagged cases where two or more particles, such as i_1 and i_2, corresponded with the same match j in the next frame. Moreover, we also ran our tracking algorithm in a reverse chronological order to detect "separation" events, the reverse of overlapping. In addition to 500 randomly chosen particle sequences, we manually examined 186 overlapping cases. After applying the algorithm above, the tracking methods successfully detected and differentiated the overlapping particles in all but two cases. This result convinced us that our approach to distinguish overlapping particles was successful.

The final challenge we needed to resolve were cases where the particles moved past a masked feature such as the bungee bar. The bar, shown in Figure 2 (A), resulted in particles leaving and the re-entering the FOV over durations that were longer than the consecutive frame interval. Here, we extended the duration of predicted centroids over 12 hours using the PIV vectors. Unpaired particles were defined as those appearing in the last of the tracking series without any matches since then. We compared the distance between the centroid of a newly arrived particle and predicted locations of unpaired particles on their estimated trajectories, based on the new arrival time. If the distance was less than 32 pixels, this newly arrived particle would undergo the same cross correlation method with other unpaired particles. Based on the same criteria described above, two particles were considered as a match if the correlation coefficient was high with a unique peak in the correlation plane.

Not all particles were traceable from their arrival through the entire deployment to the last image, and some, such as swimmers (organisms that actively entered the trap and were not part of the passive flux) were discounted from the particle flux counts. Some particles drifted off-frame, while others abruptly disappeared or had an intensity that faded below the threshold. To deal with this, we used a labeling system that indicated whether the particle disappeared at an edge, faded in FOV, or was manually identified as a swimmer. Of the 43,286 tracked particles, 10,169 were tracked from arrival to the final frame, 7,439 moved out of the FOV, 132 were categorized as large swimmers. The rest of the tracking sequences were labeled as particles faded in FOV, weak cross-correlations, and small areas. Additionally, some particles were found to enter the FOV from the sides, suggesting that they could be re-entering the image after arriving and leaving at an earlier time. Fourteen percent of the total particles were flagged as a potential re-entry. Detailed diagnoses with labels can be found in Table S1 in the supplemental materials.

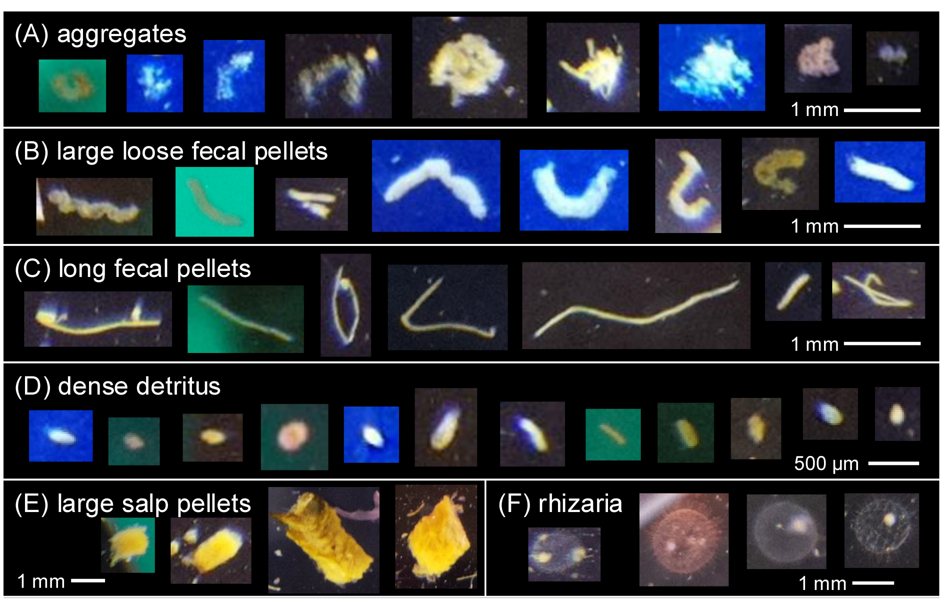

Figure 4. Passively sinking particle classes with example sub-images, including (A) aggregates, (B) large loose fecal pellets, (C) long fecal pellets, (D) dense detritus, (E) large salp pellets, and (F) rhizaria.

Particle classification

Following (Durkin et al., 2021), we classified each unique particle into one of six categories, as summarized in Figure 4. These particle categories were developed based on detailed microscope images of the same gels as those presented here. However, due to the image quality and color variations inherent in the GelCam prototype, the machine learning tools (Amaral and Durkin, 2024) that were developed for the microscope images were not optimal for these ROIs. Because of the relatively small number of GelCam images involved, and quantity of classified images needed to train a supervised model, we decided to manually assign each particle an identity based on their unprocessed colored sub-images. Aggregates had irregular shapes and loose structures and could have been clusters of phytoplankton cells and other detritus. Large loose fecal pellets were produced by large zooplankton (e.g. pterpods) and were often elongated with dense coloring. Their shapes were more regular than aggregates and composed of one or a few distinct sub units. These might be partially degraded long fecal pellets as well. Long fecal pellets were thin and elongated with smooth edges. Due to the lower pixel resolution, we classified most small ellipsoid particles as dense detritus. Following the study that has been published on the presence of salps (Bruland and Silver, 1981), we categorized their pellets as large and golden-colored, with nearly rectangular shapes. We also detected a few rhizarians, primarily Phaeodaria. Large zooplankton were occasionally observed kicking and struggling in the gel layer, and were excluded as swimmers. We differed from the classification suggested by Durkin et al. (2021), in that we did not identify any phytoplankton cells or mini pellets, since these usually had a size of less than 50 μm in ESD (Gowing and Silver, 1985), and were smaller than our detection limit.

ASSESSMENT

Modeling carbon fluxes

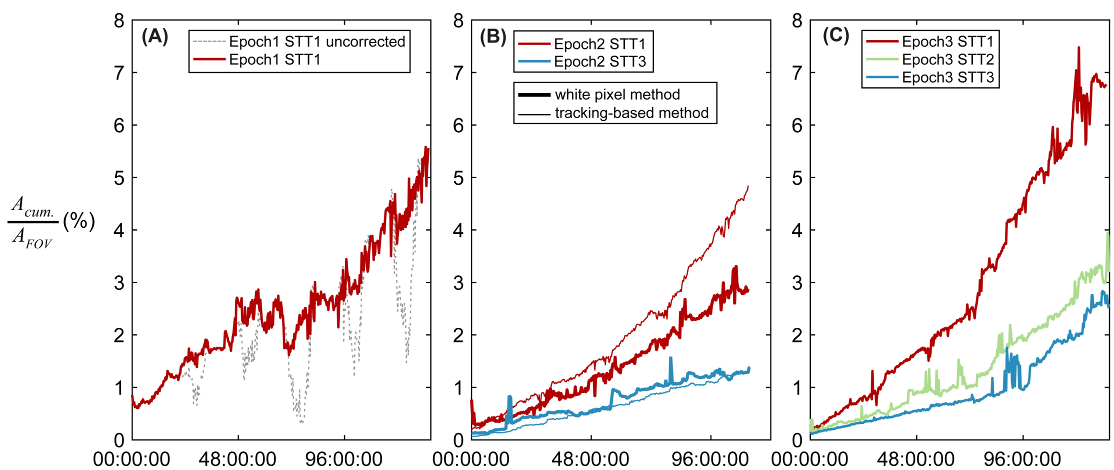

Figure 5. Cumulative particle areas as a function of time for selected samples in NP. Panel (A) consists of the number of white pixels from binarized images (dotted gray line) and the lighting-corrected cumulative areas (red solid line) during Deployment 1 STT 1. Panel (B) shows cumulative particle areas using the white pixel method (thick lines) and using the tracking-based method (thin lines) for Deployment 2 STT 1 & 3. Thin lines only focus on passively sinking particles classified following Figure 4. Panel (C) uses the white pixel method and compares the cumulative particle areas during Deployment 3. See Figure S5 for comparisons of all measurements.

Tracking “new” particle arrivals using the timelapse method enables new insights into carbon flux variability, but it also raises new challenges. Because this is a new method, with imaging tools that are still undergoing optimization, we tried two different methods for establishing an image-based carbon flux proxy. The first - hereafter referred to as the “white pixel method” - summed up the area of all white pixels in the binarized image. The white-pixel-method aims to quickly obtain the bulk particle accumulated areas using a single black-and-white threshold. This method is sensitive to the day-night variations in ambient light. Figure 5 shows the time-varying percentage FOV coverage, calculated through cumulative particle area divided by the entire FOV. Brighter ambient light conditions tended to cause an apparent reduction in size, or result in some particles dropping below the detection limit, which resulted in a drop of white pixel area during daytime (see gray line, Figure 5(A)). A linear correction was developed that utilized the difference in light intensity relative to the nighttime blue channel levels. The percentage of pixels that were “quenched” by the brighter background were then computed based on the interpolated estimate and the captured particle areas. We correlated the excessive blue light intensity with the percentage attenuation, allowing for a corrected white pixel number at each daytime time stamp (see red line, Figure 5(A)). Detailed steps for this method can be found in the supplemental materials.

While the background lighting correction did appear to correct the daytime dips in cumulative area computed via the “white pixel” method, we still observed a sharp reduction in area about 70 hours after deployment during Deployment 1 (Figure 5(A)). Review of the raw images revealed that this occurred because the trap lid bungee broke suddenly during a storm. It obscured part of the camera view, causing a flattening/decrease in the curve. Consequently, the corrected curve was composed of two nearly monotonic line segments. Similarly, deployments during

Deployment 2 and 3 showed monotonic accumulations (Figure5 B and C), despite some spikes caused by the arrival of large particles or swimmers. Overall, cumulative particle area flux decreased with depth (STT 1 was shallowest (95 - 105 m), STT 3 was deepest (195 - 205 m)).

The second method, hereafter referred to as the "tracking-based method", used a conservative version of the particle tracking and classification. We did not sum up all tracking series at their apparent time of arrival. Otherwise particles could be counted more than once due to the interruption in the tracking sequences, which was also a common issue applying the particle tracking. Rather, we implemented a frame-based calculation. Given a specific image frame with time stamp, we first found all identified particles that had been contoured. Next, we used tracking sequences to trace each particle to its state upon arrival. Using the size and shape upon arrival is intended to exclude any potential degradation or other morphological changes over time. Next, following the labeling system described above, we added all particles that left the FOV before this time stamp and subtracted particles that came into the FOV from the edges. This operation efficiently corrected the cumulative particle areas influenced by the gel movement. It is likely that this method could underestimate the particle size for those arriving during the day. However, the particle size of individual tracked particles did not show a distinct diurnal pattern.

Although it requires more processing time, an advantage of the tracking-based method over the white pixel method is that it allows an estimate of the time of arrival of particular particle types/sizes. The particulate organic carbon of each new particle was determined following the equation $C = A \cdot V^B$ listed in Durkin et al. (2021), where C is the carbon per particle (mg), A is the scaling coefficient, V is the particle volume (μm^3), and B is a unitless exponent. The exponent B characterizes the porosity of a given type of particle as its size increases. Table S2 in supplemental materials lists shapes, volumes, and modeling parameters of each particle type. We followed

Durkin et al. (2021) closely to model the POC flux. It should be noted that dense detritus were poorly resolved in our images relative to the microscope images in that paper. This particle type could be a mixed group of aggregates and fecal pellets.

After excluding air bubbles and swimmers, we extracted particle areas from the tracking series and summed all six classified categories. Figure 5(B) compares the two methods of quantifying cumulative particle areas in Deployment 2, where the symbolized curves represent the classification-based integrated areas and the others are the white-pixel-based cumulative particle areas. The two methods showed great agreement with each other, but the approach based on tracking and classification generated more smooth responses. Random spikes were eliminated because the tracking series excluded air bubbles and swimmers. These symbolized curves did not show any valley, because we only extracted particle areas at the time of arrival. In other words, using the particle tracking automatically eliminated ambient light induced area variations. Moreover, this approach accounted for particles leaving and entering the unmasked area, which also explained the small deviation from using white pixels only. See Figure S5 for measurements of all stations using both methods.

POC flux compositions and efficiency of carbon flux

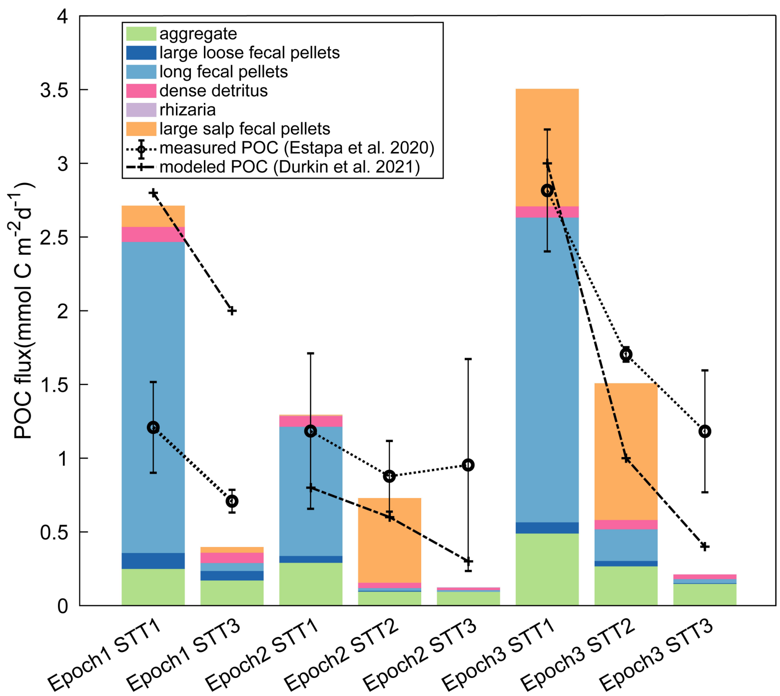

Figure 6. Modeled particulate organic carbon (POC) flux by each type during EXPORTS NP. POC fluxes are also compared with measured data in formalin-poisoned trap tubes (Estapa et al., 2021) and modeled ones based on microscopic images (Durkin et al., 2021).

The tracking based method was used to model the net POC flux for each GelCam deployment categorized according to particle type (stacked bars, Figure 6). These results are compared to the total carbon fluxes measured directly in the bulk flux tubes (open circles) and modeled POC fluxes using microscope images and classification (crosses). The details of these carbon flux methods can be found in (Estapa et al., 2021) and (Durkin et al., 2021) respectively. In general, the GelCam-modeled POC flux had fairly good agreement with the other methods in the shallower traps (STT 1 at 95m and STT 2 at 155m), and tended to underestimate the flux relative to the other measurements at STT 3 (at 205m). We suspect that a primary reason for this discrepancy at depth is that the GelCam could not resolve small particles. Particles with an equivalent diameter smaller than 100 μm could contribute up to 46% to the total POC at STT 3 during the North Pacific EXPORTS cruise (Durkin et al., 2021), whereas the detection limit was 170 μm. Additionally, visual sensors have a difficult time detecting nearly transparent or disaggregating materials as particles became further degraded with depth.

The particle-classified GelCam derived fluxes were primarily composed of aggregates, large loose fecal pellets, long fecal pellets, and dense detritus during EXPORTS-NP. Long fecal pellets were dominant at STT 1, contributing 67% to the total POC fluxes. Aggregates, large loose fecal pellets, and dense detritus were less abundant but still contributed a significant part comparing to rhazaria. At STT 3, aggregates were the most abundant, and contributed up to 70% of the total carbon. Salp pellets were observed as one of the dominant particle types in the microscope analysis of the gels (Durkin et al., 2021; Steinberg et al., 2023). Similarly, we found that large salp pellets dominated the GelCam-based POC calculations for some deployments. For example, two huge salp pellets constituted 79% of the total carbon during Deployment 2 STT 2.

Transfer efficiency was highly variable across particle types. Here we defined T_{100} as transfer efficiency, which is the ratio of carbon flux at 100 m below the reference depth (defined as the depth of STT 1) and carbon flux at the reference depth (i.e., POC_{STT3}/POC_{STT1}). The transfer efficiency in the NP were 14%, 9.6%, and 6.0%, respectively. The percentage was lower than the sediment trap measurements (Estapa et al., 2021) due to the low modeled POC fluxes at STT 3. Missing small particles could be one main reason. Long fecal pellets and large loose fecal pellets had very high attenuation (> 97.0%), showing a good agreement with the microscope analysis (Durkin et al., 2021). During Deployment 2 STT 3, we did not see any large loose fecal pellets and only 1.3% carbon of long fecal pellets remained compared to STT 1. Aggregates had the highest transfer efficiencies, which varied from 30% to 68%. One likely reason would be the conversion from other particle types and aggregation. We did not calculate the transfer efficiency of large salp fecal pellets due to the low sample number.

Episodic fluxes of fecal pellets

In contrast to traps that use only a final accumulation to estimate a time-integrated carbon flux, the GelCam provides a unique opportunity to visually examine the time series of particle fluxes during the trap deployment. One of the more striking patterns that emerged from the particle arrival and tracking analysis was the observation of diurnal fluctuations in the arrivals of fecal pellets across deployments and stations in the shallowest trap. Particle fluxes of aggregates (Figure 7(B), green line) and fecal pellets (Figure 7(B), blue line) at STT 1 were binned into two-hour time intervals and averaged into local solar time bins (operational time zone). A total of 13 days across three deployments were used for averaging the hourly fluxes. The fecal pellet fluxes included large loose and long fecal pellets only. We did not include the dense detritus, rhizaria or salp fecal pellets in the analysis. It should be noted that we also disregarded the fluxes after the mount bungee broke during Deployment 1 but kept the data before the interruption. The average fecal pellet flux reached a maximum of up to 3 mmol C m^{-2} d^{-1} occurring around 11 PM to 12 AM. After the daily maximum, the carbon fluxes from fecal pellets reduced quickly and reached less than 1 mmol C m^{-2} d^{-1}. In contrast, the aggregate fluxes did not show any distinct diurnal patterns. Because of the very strong attenuation with depth of the fecal pellet classes, we did not have enough samples to implement a statistical analysis in STT 2 and STT 3. We also observed diurnal changes in the flux of fecal pellets in the North Atlantic dataset (STT 1 at 125 m; see Figure S6). The GelCam observed the most fecal pellets during the second night and a consistent flux of aggregates over three days.

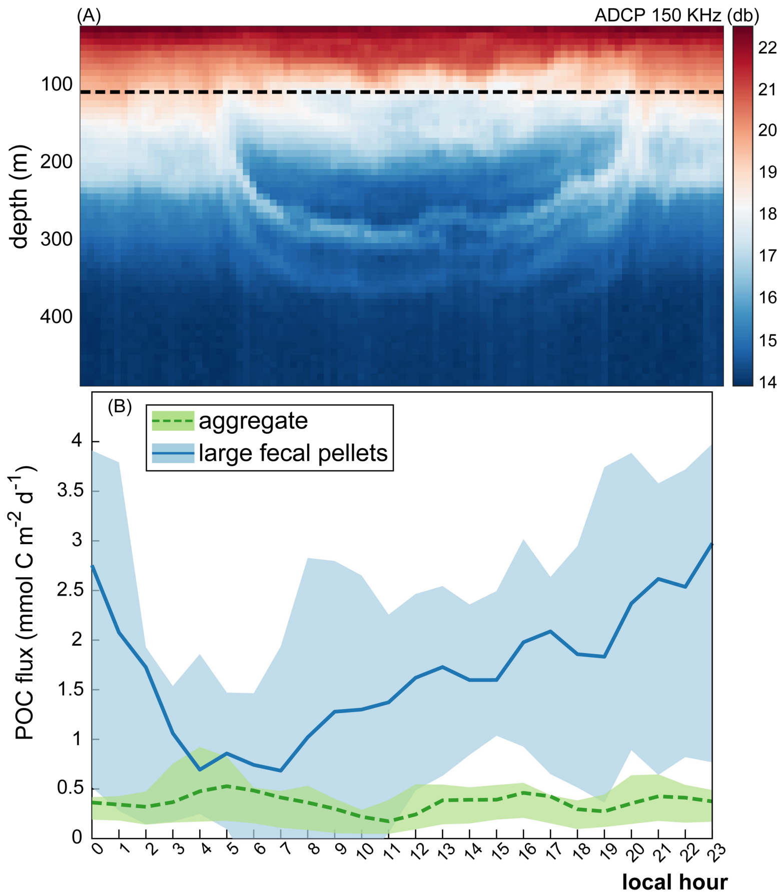

Figure 7. (A) acoustic backscattering strength from the 150 KHz ADCP with a depth range of 25 m to 500 m, shown in decibel (db). The dashed black line represents the deployment depth of GelCam at 105 m. (B) Hourly fluxes of fecal pellets in blue and aggregates in green at STT 1 during EXPORTS-NP. POC flux was averaged within a two-hour time interval. Mean values are displayed as center lines. The upper and lower boundaries of the patches represent 75th and 25th percentile of the samples.

The flux increase in fecal pellets occurring at night likely resulted from diurnal migration of zooplankton that swam to depths shallower than the trap in the upper ocean to feed at night (Cyr and Pace, 1992; Haney, 1988; Mackas and Bohrer, 1976). In Figure 7(A) the acoustic backscattering signal analyzed from the 150 KHz acoustic Doppler current profiler (ADCP) indicated higher near-surface migrator activity during the nighttime compared to day (see the anomaly of acoustic backscatter in Figure 1 from Maas et al. (2021)). Another interesting finding is that the time varying flux of fecal pellets in Figure 7 shows a skewed trend between the fecal pellet flux increase and decrease. The data suggests a sharp drop-off after midnight, with a minimum at around 6 a.m. (local) and a steady slow increase over the day.

Flux events across particle types

Flux events, sometimes called “pulse” events, have high rates of particle flux within a short time frame. To better model the biological carbon pump, it is critical to quantify these flux events (Smith et al., 2018). Bauerfind et al. (1994) observed a sharp increase of fecal pellet flux after the maximum diatom sedimentation. However, this and other studies (e.g., (Bauerfeind et al., 1994) and (Cao et al., 2024)) have conducted observations of flux events over a long time scale (from weeks to months). The use of GelCams enables measurements of flux events over timescales from hours to days. Among the GelCam deployments described in this manuscript, Deployment 3 from the North Pacific campaign (Aug. 31 - Sep. 5, 2018) provided the most complete and best quality record at all three depths. Here we examine the flux patterns of discrete particle types from the NP Deployment 3 as a function of time and depth (Figure 8). In order to highlight the temporal trends over multiple days and de-emphasize the day-and-night variation, we smoothed the flux time series using a moving average of 73 frames, equivalent to approximately 24 hours. We note that while this approach helped to highlight multi-day trends, it reduced the pattern of diel variations highlighted in Figure 7.

The flux of aggregates showed a decrease over depth consistent with the traditional Martin Curve pattern due to particle remineralization (Figure 8(A)). On average, the flux was 52% (±14% at STT 2), and 27% (±6% at STT3) of the flux at STT 1 (105 m). These ratios stayed fairly constant, even as the flux roughly tripled at all depths, varying from a minimum of 0.14 up to 1.0 mmol C $m^{-2}d^{-1}$ at STT 1 over the six day deployment. The time series of the deeper fluxes was thus correlated with the shallowest trap STT1 ($R^2 = 0.92$ ($p < 0.05$) and $R^2 = 0.84$ ($p < 0.05$) at STT 2 and STT 3, respectively).

The flux of large loose and long fecal pellets also showed an increase between the early and later stages of the deployment Figure 8(B) and (C)). The depth attenuation of large loose pellets was on average 46% between STT 2 and STT 1, and nearly 100% by STT 3 with only 8 unique particles of this type observed at 205 m. The temporal variations of large loose pellets were correlated between STT 1 and STT 2 ($R^2 = 0.31$, $p < 0.05$) and uncorrelated ($R^2 = 0.03$, $p < 0.05$) by STT3. The correlation between the shallower traps, which both showed a distinctive increase on Sep. 3 and peak on Sep. 4, lent confidence that we were resolving real short-term variations in flux that could be tracked across depth (compare the solid and short-dashed lines in Figure 8(B)).

The temporal variability in long fecal pellets at STT1 showed a similar pattern, with a gradual increase from 0.33 mmol C $m^{-2}d^{-1}$, and a peak of 4.3 mmol C $m^{-2}d^{-1}$ around 6 p.m. on Sep. 4 (Figure 8(C)). We observed a very strong depth attenuation, with a mean loss of 9.4% between STT 1 and STT 2, and 0.20% by STT 3. The time series of POC fluxes between STT 1 and STT

2 were weakly correlated with $R^2 = 0.26$ ($p < 0.05$), while the higher attenuance at STT 3 caused a lower correlation of $R^2 = 0.13$($p < 0.05$). Interestingly, we also saw a correlation between long fecal pellets and large loose pellets with R^2 of 0.39 ($p < 0.05$) at STT 1. It is plausible that there was cross-over with the labeling of these two categories and they were derived from the same origins, or that the distinct groups of animals that created the pellets were correlated with fluctuations of abundance, and thus pellet production rates.

The dense detritus category was perhaps the most confounding in terms of temporal variations (Figure 8(D)). POC flux was overall fairly low, with a range between 0.03 and 0.12 mmol C $m^{-2}d^{-1}$ at STT1. This was the only category where we observed a sustained period where the flux at STT2 exceeded that of STT1. With the data we have, it is only possible to speculate about the reason(s) for this reversal. For example, it could have been due to disaggregation of large particles into the dense detritus category between STT1 and STT2. Alternatively, there may have been a source of dense pellets located between the two traps, horizontal advection of patches, or a temporal lag that could have contributed to temporary inversions in the expected flux attenuation profile. By STT3, we observed that dense detritus were attenuated by 35% compared to the shallowest depth.

Additionally, we noticed a strong correlation between aggregates at STT 1 and dense detritus at greater depths ($R^2 = 0.91$ ($p < 0.05$) and $R^2 = 0.50$ ($p < 0.05$), respectively for STT2 and STT3). One likely reason was that the category of dense detritus were actually small aggregates or fragments. We only observed 6 rhizaria and 36 salp pellets across three depths during the six day deployment in Deployment 3. Thus correlations based on these categories were less suggestive. Tables S3 and S4 in supplemental materials show a full list of coefficients of determination between depths or particle types.

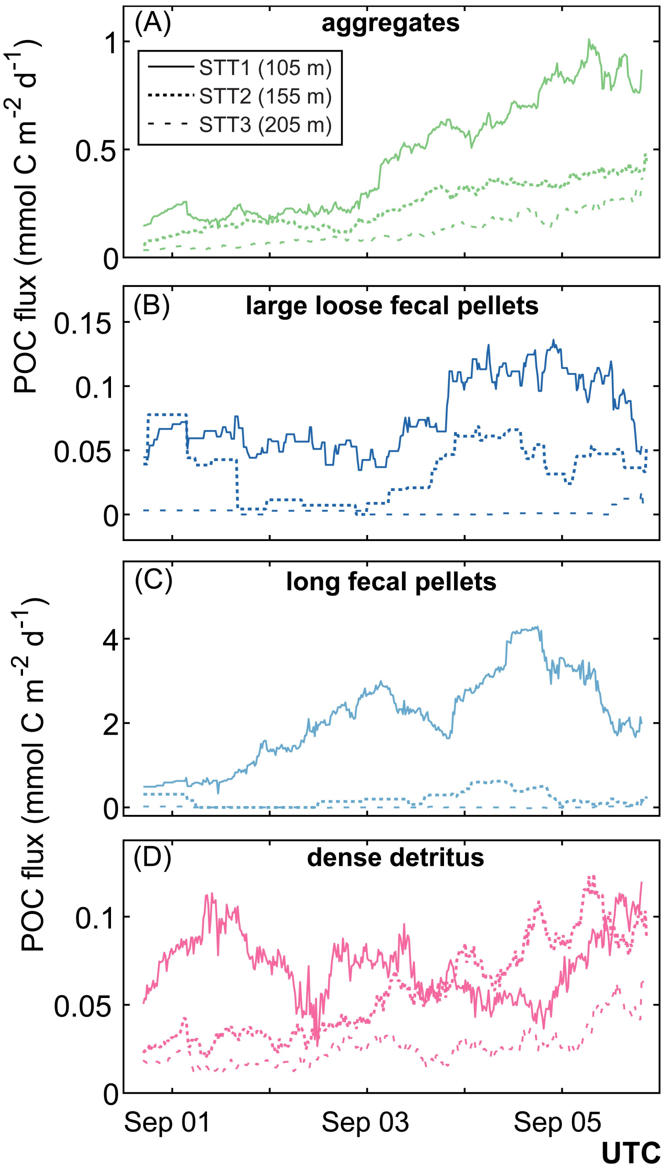

541 **Figure 8.** Time variations of POC fluxes across particle types during NP Deployment 3. Fluxes at STT 1, 2, and 3 are represented by solid, dotted, and dashed lines, respectively.

DISCUSSION

GelCams provide a new tool for observing short time variations of particle fluxes occurring within the duration of a typical surface tethered trap deployment. GelCams, when used alongside other flux measuring instruments, can be used to estimate carbon flux, and resolve episodic events and diel variations among different particle types. The modeled POC fluxes from the GelCams generally agreed with ground-truth measurements (Estapa et al., 2021; Durkin et al., 2021; Buesseler et al., 2020), although the current design cannot resolve small particles like the mini pellets described in other studies (Durkin et al., 2021). The simple, low cost, and open source design suggests that GelCams could be reproduced and attached to other platforms such as neutrally buoyant sediment traps.

Sediment traps equipped with a GelCam offer several other advantages. By taking a continuous series of photographs of the trap contents, we can observe if and when swimmers arrive, and any disruptions or changes that occur to the particles during the time spent in the trap before recovery. By tracking each individual particle over time, we can qualitatively observe if the particles are undergoing morphological changes, or if the gel is effective at preserving their size and other characteristics.

We tried two different methods to model the time-resolved particle flux from the image sequences. The white pixel method and the tracking-based methods agreed with each other in terms of the cumulative particle areas. We can choose between the two depending on the processing time and required data products. The white pixel method yielded a quick method to estimate the bulk particle flux, but was affected by background ambient light variations between day and night. We proposed a simple method to remove this effect using the red channel of the RGB image, which yielded a time series with a more monotonic increase in cumulative particle area. We can simply extract the bulk flux information and time varying fluxes in particle areas, although the carbon flux will require a further calibration incorporating particle transparency properties. This method is similar to the attenuance-flux approach employed by Estapa et al. (2024) using optical sediment traps, except the attenuance flux approach sums the attenuance values of each pixel, while the "white pixel method" here used the binarized images so each pixel had a value of unity (i.e., the method does not account for light intensities and transparency of particles). While more computationally- and labor-intensive, the particle tracking method with classification was less affected by the day-night ambient light variation, and provided information about the specific time of arrival of individual particles. These classifications allowed us to examine the relative importance of each particle type in the bulk flux, and short-term patterns (such as diel variation) and detailed temporal correlations between particle types and depths. The GelCam framework thus generates a large data set that allows for both individual case studies and statistical analysis. Recovery and subsequent analysis of the gel samples under an imaging microscope and via extraction for molecular or mineral analysis can reveal even more biological details and help with ground truthing (see (Durkin et al., 2021)).

The GelCam image series emphasizes the important role of fecal pellets in carbon flux during the EXPORTS North Pacific campaign. In agreement with previously published results (Durkin et al., 2021), long fecal pellets were the dominant particle type in the traps near the surface. The long fecal pellets and large loose fecal pellets showed rapid flux attenuation, with roughly 91% of the POC flux removed between the top two traps. Aggregates and dense detritus had higher transfer efficiencies than fecal pellets, where more complex physical and biochemical processes could significantly influence the results. Microbial degradation potentially played a more important role (Stephens et al., 2024), as small aggregates or detritus could be fragments of degraded fecal pellets. Additionally, the particle type of dense detritus could include aggregates or fecal pellets in small size. Distinguishing between them was a challenge in the GelCam images, which had a resolution approximately four times lower than the 115× microscope images published in Durkin et al. (2021). Functionally, these particle types may represent particles in a more advanced stage of microbial degradation compared to the other pellet categories. The particles that were categorized as aggregates were possibly highly degraded detritus with a loose structure. It also seems plausible that the aggregates and dense detritus in the deeper traps originated as fecal pellets at shallow depths. Moreover, physical processes including aggregation (Burd and Jackson, 2009; Kiørboe, 2001; Alldredge and Silver, 1988) and disaggregation (Briggs et al., 2020; Song et al., 2023) which can result in morphological changes as the particle sink over time, likely contributed to the uncertainty in the transfer efficiency of any particular particle class. Compared to traditional sediment trap instruments, GelCam provided unique insights into the variability of carbon flux during the trap deployments, providing a time-series with 15 minute resolution. With this record, we were able to observe diel variations in fecal pellet fluxes in the shallowest traps in both the North Pacific and North Atlantic. The diel flux peaked at midnight, likely due to the migration of zooplankton and fish to graze above the trap depth. This finding was consistent with other diel vertical migration evidence from nets and bio-acoustics (Maas et al., 2021), showing the swarming of plankton species to the surface ocean at night. A comparison using aggregates did not show any distinct diurnal changes. Analysis of 14 cumulative days of fecal pellet flux also revealed a temporal asymmetry, with a rapid three-fold drop in pellet flux between midnight and 6 a.m. (local) and then a gradual increase over the rest of the day. This asymmetrical pattern could be attributable to feeding or defecation behaviors, and further studies are required to elucidate the drivers and if similar patterns are observed in other locations.

The temporal correlations we presented in Tables S3 and S4 between trap depths are without any lag. These analyses thus assume that the processes that dictate these short timescale changes in flux are occurring simultaneously across depth. In practice however, if particles are sourced from above the shallowest trap, and take some time to sink past and into deeper traps, we might expect a time lag reflecting the vertical distance between the traps divided by the sinking speed. Previous studies using particle abundance proxies such as optical backscattering (Dall'Olmo and Mork, 2014; Briggs et al., 2011) and laser optical plankton counters (Petrik et al., 2013; Jackson et al., 2015)have shown a descending front of particles reaching successively deeper depths over time. We expected to potentially see similar results in the timing of flux events with the GelCam. Overall however, these records did not reveal obvious time lags, and so the correlations were analyzed with zero lag.

An exception to this may be qualitatively evident in the GelCam timeseries from STT 1 and 3 from Deployment 3 EXPORTS-NP (see Figure 5(C) and Figure 8(A)). In Figure 5(C), we observed that the total cumulative particle areas all had a noticeable slope shift, with an increase at STT 1 (105 m) around 75 hours after the deployment while the slope of STT 3 (205 m) did not increase until 96 hours. This shift in slope provided a bulk sinking speed of roughly 100 m/day. The particle classifications suggest that the increase was partially driven by aggregates (Figure 8(A)). Dividing the vertical distance between STT 1 and 3, by the time lag, we achieve a roughly estimated sinking speed of 50 m/day for aggregates. The estimated sinking speeds of bulk particles or aggregates fall within the range of another study on the same cruise (Romanelli et al., 2024) and previous studies (McDonnell and Buesseler, 2010; Fowler and Small, 1972; Trull et al., 2008; Ploug et al., 2008). The absence of this pattern for other particle types could be indicative of faster sinking speeds, though our data was not sufficient to make a conclusive assessment of this hypothesis. We anticipate that future GelCam studies will allow more robust observations of these dynamics.

The GelCam system is a promising tool for providing high temporal resolution flux, but it also has a number of limitations that could be addressed with future technical improvements. A primary challenge was the low pixel resolution and variability in illumination, which can be improved in the future. In this study, we could not determine cumulative mini fecal pellets, as their size was smaller than one pixel. Additionally, particle classification had high uncertainty for small particles that just passed the detection threshold. For example, long fecal pellets, or fibers could be misidentified due to inadequate details. Durkin et al. (2021) noted aggregates as one dominant population in the Subarctic North Pacific, but many aggregates were lost during the identification process because of their loose structures and transparent exopolymer particles (TEP) (Passow, 2002; Azetsu-Scott and Passow, 2004). Inevitably, we could not account for the contributions of organic carbon from TEP.

Salp fecal pellets were found to be abundant during EXPORTS-NP (Durkin et al., 2021; Stamieszkin et al., 2021), but we could only resolve ones with large sizes due to over-saturated colors in small particles. We observed very few large salp pellets but these large particles could substantially affect the modeling of POC fluxes (e.g., Deployment 2 STT 2). Since we only deployed one GelCam at each depth, with a sampling area of $< 30cm^2$, the limitation could cause high variability of rhizaria and large salp pellets, collected from different sediment trap tubes. These rare occurrences compared to large numbers of other particles suggests that the deployment of larger numbers of GelCams and other particle-intercepting sediment traps could improve collection statistics. Fortunately the low cost of GelCam could make it possible in the future. Additionally, smaller salp pellets were usually classified into aggregates or detritus. We could minimize this uncertainty by resolving particle color in the next development iteration.

We only resolved 2D images of particles from the single-camera imaging system. While we could predict thickness of particles that retained regular shapes, such as long fecal pellets, particles prone to flattening within the gel would have more biased thickness predictions. These particles, such as especially delicate aggregates, tend to flatten and extend their projection areas when resting on a platform, thus leading to the overestimation of thickness based on assumptions of spherical shapes. In addition to uncalibrated 3D morphological information, 2D images resulted in the overlap of sub-images. For future improvements, capturing an additional view for 3D volume reconstruction, or establishing an empirical relationship for aggregate thickness, would be advantageous.

Hardware upgrades will enhance the GelCam design in the future. For instance, in EXPORTS-NA, we encountered images with a blue hue, but new GelCam models will send fixed parameters to the Pi camera to ensure calibrated white balance. Upgrading to more advanced camera modules with attached lenses will also generate a higher pixel resolution. Although it is still challenging to detect mini fecal pellets ($< 50\ \mu m$), these improvements can reduce the detection limit of the imaging system. We are also exploring the integration of GelCam with Langrangian floats. As Siegel and Deuser (1997) demonstrated, horizontal bulk flow is normally orders of magnitude greater than the sinking velocity, so replacing the surface tethered traps (STT) with neutrally buoyant sediment traps (NBST) will lead to a more precise flux measurement within the water column. Furthermore, incorporating a swimmer exclusion device (e.g. the "labyrinth of doom" (Coale, 1990)) could still be favorable. Although we could exclude them during the post processing, the swimming zooplankton brought more uncertainty in PIV analysis and they may potentially interact with other particles.

The white pixel method can be further developed by building an empirical relation to the POC fluxes. This idea is not new, as Bishop et al. (2016) estimated the carbon fluxes by empirically relating thickness of particles to their projection areas and converting the particle volume into the carbon content. Similarly, Estapa et al. (2024) empirically correlated the light attenuance of particles with the POC fluxes. We did not apply any of these empirical relations, because particles were illuminated from the side (not behind as required for an attenuance estimate), particle areas were corrected based on lighting, and particles preserved in the gel layer did not become fully flattened due to gravity. Building a reliable relation requires an extensive datasets collected by GelCam and other similar instruments featuring upward facing cameras and side lighting (i.e., quasi-darkfield illumination). Alternatively, we could utilize the other tracking-based method for more accurate POC flux estimation than an empirical relation. The tracking-based and white-pixel-based methods are interchangeable depending on the specific purpose.

Implementing an automated particle classification process will be beneficial, to reduce the labor of processing sub-images manually. Leveraging machine learning methods will provide significant insights into the model of carbon export(Irisson et al., 2022; Trudnowska et al., 2021; Amaral and Durkin, 2024). For example, Davies et al. (2017) applied a deep convolutional neural network (CNN) to classify particles, including larvae, copepod, and oil droplets, in an in situ imaging system. However, many classifiers are still constrained by the limited size of available particle image datasets (Irisson et al., 2022). We believe machine learning methods and GelCam will have a mutually beneficial relationship in the future. On one side, machine learning will enhance the particle identification capabilities of the GelCam. More importantly, as a low-cost but reliable instrument, the GelCam records a wide range of particle types, which will generate a larger database of particle images and improve the accuracy of machine learning classifiers.

Future work can expand the GelCam in more studies of the biological carbon pump. The polyacrylamide gel layer maintains particle structure during sample collection, therefore we can incorporate more GelCams in various directions to capture the 3D shape. By removing the gel layer from the sediment trap, we can track marine particles without interfering with natural biological processes. This adjustment would enable visual quantification of microbial degradation rates acting on fecal pellets and aggregates. In other words, this modified instrument will potentially allow observations of time varying morphological changes or even fragmentation. Additionally, continuing to deploy GelCams with traditional sediment traps at different locations, seasons, and depths will not only yield estimates of a bulk particle sinking velocity but also provide more insights into the varying settling behaviors across different particle types.

ACKNOWLEDGMENTS

Data collected through this project was supported by NASA Grants 80NSSC17K0662 and 80NSSC21K0015.

Postdoctoral support for YS was provided by Oceankind foundation. We wish to thank Dr. Nils Haentjens, Dr. Vinicius Amaral, Roger Patrick Kelly, Sean O'Neil, Dr. Alyson Santoro, Nicola Paul, and the EXPORTS team for assistance with data collection, their helpful discussions and constructive recommendations. We are also grateful to captains and crew of the R/V Revelle and R/V James Cook.

CONFLICT OF INTEREST

None declared.

REFERENCES

Alldredge, A. L. and Gotschalk, C. (1988). In situ settling behavior of marine snow1. *Limnology and Oceanography*, 33(3):339–351.

Alldredge, A. L. and Silver, M. W. (1988). Characteristics, dynamics and significance of marine snow. *Progress in Oceanography*, 20(1).

Amaral, V. J. and Durkin, C. A. (2024). A computer vision-based approach for estimating carbon fluxes from sinking particles in the ocean. *bioRxiv*.

Azetsu-Scott, K. and Passow, U. (2004). Ascending marine particles: Significance of transparent exopolymer particles (TEP) in the upper ocean. *Limnology and Oceanography*, 49(3):741–748.

Basu, S. and Mackey, K. (2018). Phytoplankton as Key Mediators of the Biological Carbon Pump: Their Responses to a Changing Climate. *Sustainability*, 10(3):869.

Bauerfeind, E., Bodungen, B., Arndt, K., and Koeve, W. (1994). Particle flux, and composition of sedimenting matter, in the Greenland Sea. *Journal of Marine Systems*, 5(6):411–423.

Bishop, J. K. B., Fong, M. B., and Wood, T. J. (2016). Robotic observations of high wintertime carbon export in California coastal waters. *Biogeosciences*, 13(10):3109–3129.

Briggs, N., Dall'Olmo, G., and Claustre, H. (2020). Major role of particle fragmentation in regulating biological sequestration of CO2 by the oceans. *Science*, 367(6479):791–793.

Briggs, N., Perry, M. J., Cetinic, I., Lee, C., D'Asaro, E., Gray, A. M., and Rehm, E. (2011). High-´ resolution observations of aggregate flux during a sub-polar North Atlantic spring bloom. *Deep Sea Research Part I: Oceanographic Research Papers*, 58(10):1031–1039.

Bruland, K. W. and Silver, M. W. (1981). Sinking rates of fecal pellets from gelatinous zooplankton (Salps, Pteropods, Doliolids). *Marine Biology*, 63(3):295–300.

Buesseler, K. O., Antia, A. N., Chen, M., Fowler, S. W., Gardner, W. D., Gustafsson, O., Harada, K., Michaels, A. F., Rutgers van der Loeff, M., Sarin, M., Steinberg, D. K., and Trull, T. (2007). An assessment of the use of sediment traps for estimating upper ocean particle fluxes. *Journal of Marine Research*, 65(3):345–416.

Buesseler, K. O., Benitez-Nelson, C. R., Roca-Mart´ı, M., Wyatt, A. M., Resplandy, L., Clevenger, S. J., Drysdale, J. A., Estapa, M. L., Pike, S., and Umhau, B. P. (2020). High-resolution spatial and temporal measurements of particulate organic carbon flux using thorium-234 in the northeast Pacific Ocean during the EXport Processes in the Ocean from RemoTe Sensing field campaign. *Elementa: Science of the Anthropocene*, 8(1).

Burd, A. B. and Jackson, G. A. (2009). Particle Aggregation. *Annual Review of Marine Science*, 1(1):65–90.

Cao, J., Liu, Z., Lin, B., Zhao, Y., Li, J., Wang, H., Zhang, X., Zhang, J., and Song, H. (2024). Temporal and vertical variations in carbon flux and export of zooplankton fecal pellets in the western South China Sea. *Deep Sea Research Part I: Oceanographic Research Papers*, 207:104283.

Cavan, E. L., Henson, S. A., Belcher, A., and Sanders, R. (2017). Role of zooplankton in determining the efficiency of the biological carbon pump. *Biogeosciences*, 14(1):177–186.

Cavan, E. L., Le Moigne, F. A. C., Poulton, A. J., Tarling, G. A., Ward, P., Daniels, C. J., Fragoso, G. M., and Sanders, R. J. (2015). Attenuation of particulate organic carbon flux in the Scotia Sea, Southern Ocean, is controlled by zooplankton fecal pellets. *Geophysical Research Letters*, 42(3):821–830.

Coale, K. H. (1990). Labyrinth of doom: A device to minimize the “swimmer” component in sediment trap collections. *Limnology and Oceanography*, 35(6):1376–1381.

Collins, J. R., Edwards, B. R., Thamatrakoln, K., Ossolinski, J. E., DiTullio, G. R., Bidle, K. D., Doney, S. C., and Van Mooy, B. A. S. (2015). The multiple fates of sinking particles in the North Atlantic Ocean. *Global Biogeochemical Cycles*, 29(9):1471–1494.

Cyr, H. and Pace, M. L. (1992). Grazing by Zooplankton and Its Relationship to Community Structure. *Canadian Journal of Fisheries and Aquatic Sciences*, 49(7):1455–1465.

Dall'Olmo, G. and Mork, K. A. (2014). Carbon export by small particles in the Norwegian Sea. *Geophysical Research Letters*, 41(8):2921–2927.

Davies, E., Brandvik, P., Leirvik, F., and Nepstad, R. (2017). The use of wide-band transmittance imaging to size and classify suspended particulate matter in seawater. *Marine Pollution Bulletin*, 115(1-2):105–114.

De La Rocha, C. L. and Passow, U. (2007). Factors influencing the sinking of POC and the efficiency of the biological carbon pump. *Deep Sea Research Part II: Topical Studies in Oceanography*, 54(57):639–658.

Durkin, C. A., Buesseler, K. O., Cetinic, I., Estapa, M. L., Kelly, R. P., and Omand, M. (2021). A Visual´ Tour of Carbon Export by Sinking Particles. *Global Biogeochemical Cycles*, 35(10).

Durkin, C. A., Van Mooy, B. A. S., Dyhrman, S. T., and Buesseler, K. O. (2016). Sinking phytoplankton associated with carbon flux in the Atlantic Ocean. *Limnology and Oceanography*, 61(4):1172–1187.

Estapa, M., Buesseler, K., Durkin, C. A., Omand, M., Benitez-Nelson, C. R., Roca-Mart´ı, M., Breves,

E., Kelly, R. P., and Pike, S. (2021). Biogenic sinking particle fluxes and sediment trap collection efficiency at Ocean Station Papa. *Elementa: Science of the Anthropocene*, 9(1).

Estapa, M. L., Durkin, C. A., Slade, W. H., Huffard, C. L., O’Neill, S. P., and Omand, M. M. (2024). A new, global optical sediment trap calibration. *Limnology and Oceanography: Methods*, 22(2):77–92.

Fowler, S. W. and Knauer, G. A. (1986). Role of large particles in the transport of elements and organic compounds through the oceanic water column. *Progress in Oceanography*, 16(3):147–194.

Fowler, S. W. and Small, L. F. (1972). Sinking Rates of Euphausiid fecal pellets. *Limnology and Oceanography*, 17(2):293–296.

Friedlingstein, P., O’Sullivan, M., Jones, M. W., Andrew, R. M., Bakker, D. C. E., Hauck, J., Landschutzer,¨ P., Le Quer´ e, C., Luijkx, I. T., Peters, G. P., Peters, W., Pongratz, J., Schwingshackl, C., Sitch, S.,´ Canadell, J. G., Ciais, P., Jackson, R. B., Alin, S. R., Anthoni, P., Barbero, L., Bates, N. R., Becker, M., Bellouin, N., Decharme, B., Bopp, L., Brasika, I. B. M., Cadule, P., Chamberlain, M. A., Chandra, N., Chau, T.-T.-T., Chevallier, F., Chini, L. P., Cronin, M., Dou, X., Enyo, K., Evans, W., Falk, S., Feely, R. A., Feng, L., Ford, D. J., Gasser, T., Ghattas, J., Gkritzalis, T., Grassi, G., Gregor, L., Gruber, N., Gurses, O., Harris, I., Hefner, M., Heinke, J., Houghton, R. A., Hurtt, G. C., Iida, Y., Ilyina, T.,¨ Jacobson, A. R., Jain, A., Jarn´ıkova, T., Jersild, A., Jiang, F., Jin, Z., Joos, F., Kato, E., Keeling, R. F.,´ Kennedy, D., Klein Goldewijk, K., Knauer, J., Korsbakken, J. I., Kortzinger, A., Lan, X., Lef˙ evre,` N., Li, H., Liu, J., Liu, Z., Ma, L., Marland, G., Mayot, N., McGuire, P. C., McKinley, G. A., Meyer, G., Morgan, E. J., Munro, D. R., Nakaoka, S.-I., Niwa, Y., O’Brien, K. M., Olsen, A., Omar, A. M., Ono, T., Paulsen, M., Pierrot, D., Pocock, K., Poulter, B., Powis, C. M., Rehder, G., Resplandy, L., Robertson, E., Rodenbeck, C., Rosan, T. M., Schwinger, J., S¨ ef´ erian, R., Smallman, T. L., Smith, S. M.,´ Sospedra-Alfonso, R., Sun, Q., Sutton, A. J., Sweeney, C., Takao, S., Tans, P. P., Tian, H., Tilbrook, B., Tsujino, H., Tubiello, F., van der Werf, G. R., van Ooijen, E., Wanninkhof, R., Watanabe, M., Wimart-Rousseau, C., Yang, D., Yang, X., Yuan, W., Yue, X., Zaehle, S., Zeng, J., and Zheng, B. (2023). Global Carbon Budget 2023. *Earth System Science Data*, 15(12):5301–5369.

Gowing, M. M. and Silver, M. W. (1985). Minipellets: A new and abundant size class of marine fecal pellets. *Journal of Marine Research*, 43(2):395–418.

Haney, J. F. (1988). Diel patterns of zooplankton behaviour. *Bulletin of Marine Science*, 43(3):583–603.

Henson, S. A., Sanders, R., Madsen, E., Morris, P. J., Le Moigne, F., and Quartly, G. D. (2011). A reduced estimate of the strength of the ocean's biological carbon pump. *Geophysical Research Letters*, 38(4).

Irisson, J.-O., Ayata, S.-D., Lindsay, D. J., Karp-Boss, L., and Stemmann, L. (2022). Machine Learning for the Study of Plankton and Marine Snow from Images. *Annual Review of Marine Science*, 14(1):277–301.

Jackson, G. A., Checkley, D. M., and Dagg, M. (2015). Settling of particles in the upper 100 m of the ocean detected with autonomous profiling floats off California. *Deep Sea Research Part I: Oceanographic Research Papers*, 99:75–86.

Kiørboe, T. (2001). Formation and fate of marine snow: small-scale processes with large- scale implications. *Scientia Marina*, 65(S2).

Maas, A. E., Miccoli, A., Stamieszkin, K., Carlson, C. A., and Steinberg, D. K. (2021). Allometry and the calculation of zooplankton metabolism in the subarctic Northeast Pacific Ocean. *Journal of Plankton Research*, 43(3):413–427.

Mackas, D. and Bohrer, R. (1976). Fluorescence analysis of zooplankton gut contents and an investigation of diel feeding patterns. *Journal of Experimental Marine Biology and Ecology*, 25(1):77–85.

McDonnell, A. M. P. and Buesseler, K. O. (2010). Variability in the average sinking velocity of marine particles. *Limnology and Oceanography*, 55(5):2085–2096.

Mendez, M., Raiola, M., Masullo, A., Discetti, S., Ianiro, A., Theunissen, R., and Buchlin, J.-M. (2017).

POD-based background removal for particle image velocimetry. *Experimental Thermal and Fluid Science*, 80.

Middelburg, J. J. (2011). Chemoautotrophy in the ocean. *Geophysical Research Letters*, 38(24).

Muller, P. and Suess, E. (1979). Productivity, sedimentation rate, and sedimentary organic matter in the¨ oceans—I. Organic carbon preservation. *Deep Sea Research Part A. Oceanographic Research Papers*, 26(12):1347–1362.

Muller-Karger, F. E. (2005). The importance of continental margins in the global carbon cycle. *Geophysical Research Letters*, 32(1).

Nobach, H. and Honkanen, M. (2005). Two-dimensional Gaussian regression for sub-pixel displacement estimation in particle image velocimetry or particle position estimation in particle tracking velocimetry. *Experiments in Fluids*, 38(4):511–515.

Nowicki, M., DeVries, T., and Siegel, D. A. (2022). Quantifying the Carbon Export and Sequestration Pathways of the Ocean's Biological Carbon Pump. *Global Biogeochemical Cycles*, 36(3).

Omand, M. M., D'Asaro, E. A., Lee, C. M., Perry, M. J., Briggs, N., Cetinic, I., and Mahadevan, A.´ (2015). Eddy-driven subduction exports particulate organic carbon from the spring bloom. *Science*, 348(6231):222–225.

Otsu, N. (1979). A Threshold Selection Method from Gray-Level Histograms. *IEEE Transactions on Systems, Man, and Cybernetics*, 9(1).

Passow, U. (2002). Transparent exopolymer particles (TEP) in aquatic environments. *Progress in Oceanography*, 55(3-4):287–333.

Petrik, C. M., Jackson, G. A., and Checkley, D. M. (2013). Aggregates and their distributions determined from LOPC observations made using an autonomous profiling float. *Deep Sea Research Part I: Oceanographic Research Papers*, 74:64–81.

Piao, S., Sitch, S., Ciais, P., Friedlingstein, P., Peylin, P., Wang, X., Ahlstrom, A., Anav, A., Canadell,¨ J. G., Cong, N., Huntingford, C., Jung, M., Levis, S., Levy, P. E., Li, J., Lin, X., Lomas, M. R., Lu, M., Luo, Y., Ma, Y., Myneni, R. B., Poulter, B., Sun, Z., Wang, T., Viovy, N., Zaehle, S., and Zeng, N. (2013). Evaluation of terrestrial carbon cycle models for their response to climate variability and to ¡scp¿ ¡scp¿ CO ¡sub¿2¡/sub¿ ¡/scp¿ ¡/scp¿ trends. *Global Change Biology*, 19(7):2117–2132.

Ploug, H., Iversen, M. H., and Fischer, G. (2008). Ballast, sinking velocity, and apparent diffusivity within marine snow and zooplankton fecal pellets: Implications for substrate turnover by attached bacteria. *Limnology and Oceanography*, 53(5):1878–1886.

Romanelli, E., Giering, S., Estapa, M., Siegel, D., and Passow, U. (2024). Intense storms affect sinking particle fluxes after the North Atlantic diatom spring bloom. *bioRxiv*.

Siegel, D. and Deuser, W. (1997). Trajectories of sinking particles in the Sargasso Sea: modeling of statistical funnels above deep-ocean sediment traps. *Deep Sea Research Part I: Oceanographic Research Papers*, 44(9-10):1519–1541.

Siegel, D. A., Cetinic, I., Graff, J. R., Lee, C. M., Nelson, N., Perry, M. J., Ramos, I. S., Steinberg, D. K.,´ Buesseler, K., Hamme, R., Fassbender, A. J., Nicholson, D., Omand, M. M., Robert, M., Thompson, A., Amaral, V., Behrenfeld, M., Benitez-Nelson, C., Bisson, K., Boss, E., Boyd, P. W., Brzezinski, M., Buck, K., Burd, A., Burns, S., Caprara, S., Carlson, C., Cassar, N., Close, H., D’Asaro, E., Durkin, C., Erickson, Z., Estapa, M. L., Fields, E., Fox, J., Freeman, S., Gifford, S., Gong, W., Gray, D., Guidi, L., Haentjens, N., Halsey, K., Huot, Y., Hansell, D., Jenkins, B., Karp-Boss, L., Kramer, S., Lam,¨ P., Lee, J.-M., Maas, A., Marchal, O., Marchetti, A., McDonnell, A., McNair, H., Menden-Deuer, S., Morison, F., Niebergall, A. K., Passow, U., Popp, B., Potvin, G., Resplandy, L., Roca-Mart´ı, M., Roesler, C., Rynearson, T., Traylor, S., Santoro, A., Seraphin, K. D., Sosik, H. M., Stamieszkin, K., Stephens, B., Tang, W., Van Mooy, B., Xiong, Y., and Zhang, X. (2021). An operational overview of the EXport Processes in the Ocean from RemoTe Sensing (EXPORTS) Northeast Pacific field deployment. *Elementa: Science of the Anthropocene*, 9(1).

SierraI, C. A., Harmon, M. E., Moreno, F. H., Orrego, S. A., and Del Valle, J. I. (2007). Spatial and temporal variability of net ecosystem production in a tropical forest: testing the hypothesis of a significant carbon sink. *Global Change Biology*, 13(4):838–853.

Smith, K. L., Ruhl, H. A., Huffard, C. L., Messie, M., and Kahru, M. (2018). Episodic organic carbon´ fluxes from surface ocean to abyssal depths during long-term monitoring in NE Pacific. *Proceedings of the National Academy of Sciences*, 115(48):12235–12240.

Song, Y., Burd, A. B., and Rau, M. J. (2023). The deformation of marine snow enables its disaggregation in simulated oceanic shear. *Frontiers in Marine Science*, 10.

Song, Y. and Rau, M. J. (2022). A novel method to study the fragmentation behavior of marine snow aggregates in controlled shear flow. *Limnology and Oceanography: Methods*, 20(10):618–632.

Stamieszkin, K., Steinberg, D. K., and Maas, A. E. (2021). Fecal pellet production by mesozooplankton in the subarctic Northeast Pacific Ocean. *Limnology and Oceanography*, 66(7):2585–2597.

Steinberg, D. K., Stamieszkin, K., Maas, A. E., Durkin, C. A., Passow, U., Estapa, M. L., Omand, M. M., McDonnell, A. M. P., Karp-Boss, L., Galbraith, M., and Siegel, D. A. (2023). The Outsized Role of Salps in Carbon Export in the Subarctic Northeast Pacific Ocean. *Global Biogeochemical Cycles*, 37(1).

Stephens, B. M., Durkin, C. A., Sharpe, G., Nguyen, T. T. H., Albers, J., Estapa, M. L., Steinberg, D. K., Levine, N. M., Gifford, S. M., Carlson, C. A., Boyd, P. W., and Santoro, A. E. (2024). Direct observations of microbial community succession on sinking marine particles. *The ISME Journal*, 18(1).

Thielicke, W. and Stamhuis, E. J. (2014). PIVlab – Towards User-friendly, Affordable and Accurate Digital Particle Image Velocimetry in MATLAB. *Journal of Open Research Software*, 2.

Trudnowska, E., Lacour, L., Ardyna, M., Rogge, A., Irisson, J. O., Waite, A. M., Babin, M., and Stemmann, L. (2021). Marine snow morphology illuminates the evolution of phytoplankton blooms and determines their subsequent vertical export. *Nature Communications*, 12(1):2816.

Trull, T., Bray, S., Buesseler, K., Lamborg, C., Manganini, S., Moy, C., and Valdes, J. (2008). In situ measurement of mesopelagic particle sinking rates and the control of carbon transfer to the ocean interior during the Vertical Flux in the Global Ocean (VERTIGO) voyages in the North Pacific. *Deep Sea Research Part II: Topical Studies in Oceanography*, 55(14-15):1684–1695.

Turner, J. (2002). Zooplankton fecal pellets, marine snow and sinking phytoplankton blooms. *Aquatic Microbial Ecology*, 27:57–102.

Westerweel, J. and Scarano, F. (2005). Universal outlier detection for PIV data. *Experiments in Fluids*, 39:1096–1100.

Data Availability Statement

The data that support the findings of this study are openly available in in NASA's SeaBASS archive at https://oceandata.sci.gsfc.nasa.gov/ob/getfile/dd2fe323be_EXPORTS-EXPORTSNP_RR1813_GelCam_20180814-20180909_R1.sb and https://oceandata.sci.gsfc.nasa.gov/ob/getfile/8a0152ccab_EXPORTS-EXPORTSNA_JC214_GelCam_20210504-20210509_R1.sb.

SUPPLEMENTAL MATERIALS

Camera calibration

As the camera viewed through layers of acrylics and polyacrylamide gel, we printed a calibration target as shown in Figure S1 in order to measure the magnification ratio and reconstruct undistorted images. The calibration plate consisted of a grid of black dots used for establishing a mapping between the image and the real coordinates. Larger dots had a diameter of 2 mm with a spacing of 10 mm, while the diameter of smaller dots was 1 mm. During the calibration, the target was placed onto the top surface of the GelCam housing, which was also the bottom of the gel layer. Making sure the target was covering the entire field of view, we then captured the image of the calibration target. With a simple binarization, we computed centers of all black dots and mapped their locations with real coordinates. The distortion effects were corrected by fitting a polynomial function. As a result, we could estimate the pixel size in any location of captured images. The average magnification was 21.3 μm per pixel during EXPORTS 2018 and 25.3 μm per pixel during EXPORTS 2021.

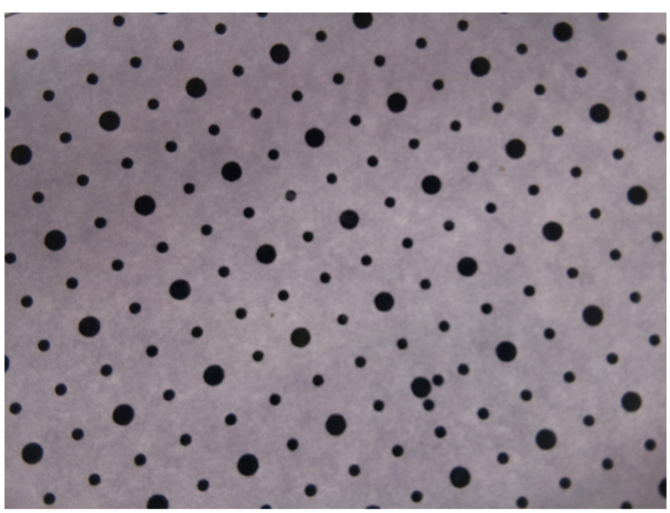

Figure S1. Calibration image used for calculating magnification and correcting distortion during EXPORTS 2021.

Summary of tracking sequences and labeling system

Table S1 presents the number of binarized particles and tracking results from ten deployments. The shallowest depth, STT 1, recorded the most particles, while measurements in STT 2 observed half as many particles as STT 1. With a time interval of approximately 20 minutes, our tracking algorithm successfully monitored particles for more than ten hours (~30 frames) on average. Excluding fast-moving zooplankton, air bubbles, and other misidentified particles, the tracking duration could be further improved for particles categorized in Figure 4.

We employed a numerical labeling system to categorize various situations when the particle tracking was ceased. Specifically, the notation "-1" denoted instances when particles were leaving the FOV. Whenever no particle was successfully matched, and the best correlation coefficient was smaller than 0.5, we identified these cases using the label "-2". The label "-3" was assigned when we could not find a matched particle, particularly when the particle's area in the preceding frame was less than 100 pixels ($ESD \sim 240 \mu m$). Another distinct scenario arose when we failed to track a particle due to its insufficient average gray scale intensity lower than the global Otsu's threshold. In such cases, we marked the particle with the label "-4". Occasionally, we encountered moving zooplankton during our analysis, leading to the assignment of a "-5" flag. The notation "-6" represented all other situations where the tracking process was lost or unsuccessful. Lastly, we defined a "-7" where a particle was entering the FOV from the outside. The label "-7" was generated in a same way as "-1", when we ran the tracking algorithm in a reverse chronological order. These designated labels enabled a systematic characterization of the diverse outcomes encountered throughout our investigation.

Table S1. Summary of particle tracking. Binarized particles represent particles contoured and preprocessed for tracking. Tracking particles include all particle categories with zooplankton and air bubbles, before performing a classification. Average tracking frames correspond to the mean duration of tracking. Each frame represents a time interval of 20 minutes approximately.

Deployments		Contoured particles	Tracking sequences	-1 leaving FOV	-2 weak correlation	-3 small areas	-4 dim particles	-5 large swimmer	-6 others	-7 entering FOV
NP Epoch1	STT1	118,775	13,786	3,244	3,827	1,731	937	90	1,926	2,180
	STT2	N.A.	N.A.	N.A.	N.A.	N.A.	N.A.	N.A.	N.A.	N.A.
	STT3	100,585	10,193	1,166	3,062	2,025	235	17	1,687	1,180
NP Epoch2	STT1	84,908	3,525	681	456	634	302	14	318	469
	STT2	41,586	1,580	240	348	454	62	2	137	207
	STT3	28,626	1,404	234	366	347	87	3	152	174
NP Epoch3	STT1	176,828	5,423	845	402	862	250	0	30	704
	STT2	94,347	3,328	758	571	673	93	4	296	583
	STT3	57,579	2,810	108	65	137	15	0	36	396
NA		32,068	1,184	163	89	300	169	2	58	100

Lighting correction of the white pixel method

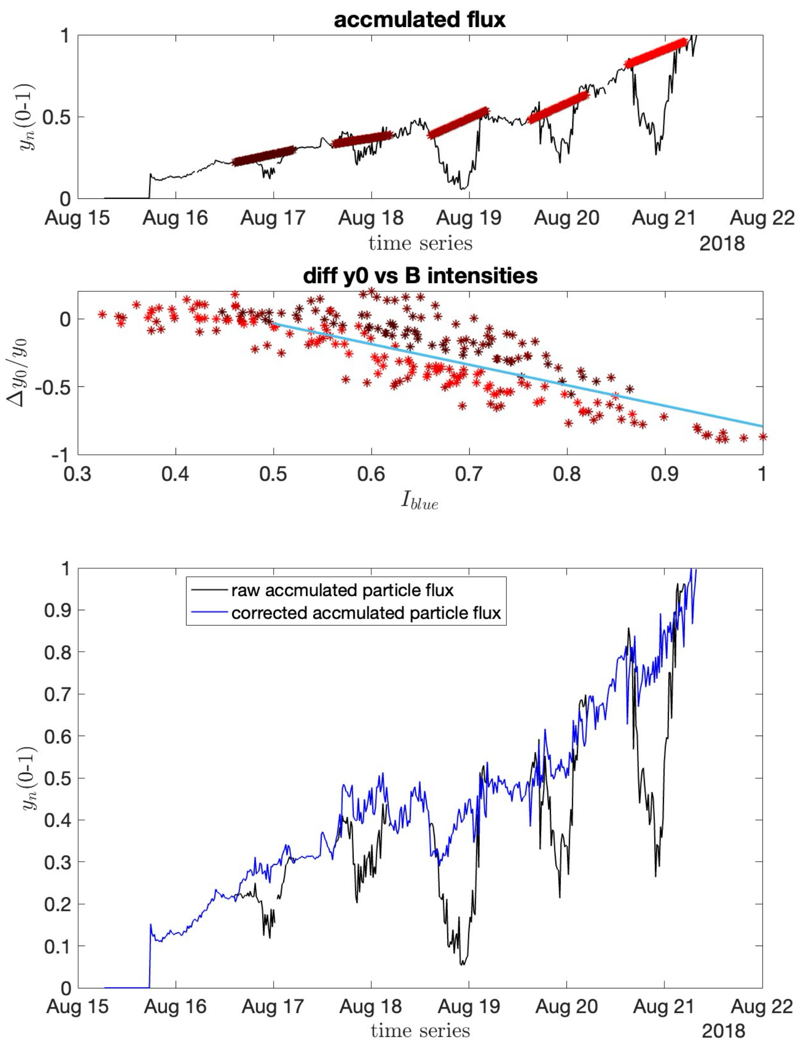

Figure S2. Correction of the cumulative particle areas in white pixels. (a) linear interpolation during the nighttime, (b) linear fitting of the percentage attenuation against the blue light intensities, and (c) corrected number of white pixels.

We estimated the total area of deposited particles using grayscale images, which we derived from the red-channel image after the background subtraction. Again we applied the global Otsu's black-andwhite threshold. The number of white pixels that exceeded the global Otsu threshold provided a quick approximation of the total deposited particles. However, the presence of ambient light, especially at shallow depths, posed a challenge, as high ambient lighting intensities could lead to the underestimation of particle sizes due to light scattering effects.

To tackle this challenge, we developed a correction method based on the ambient lighting intensity. As highlighted in the section above, the predominant background illuminations were observed in the green and blue channels. Here we defined excessive blue light intensity as the difference in light intensity from the nighttime blue channel. By definition, the excessive intensity reached the maximum around noon. Based on the observation that particle areas became smaller under stronger ambient light, we assumed that the excessive intensity was linearly correlated with the percentage decrease in binarized particle area. It should be noted that the blue channel was used because the area attenuation was slightly more sensitive than the green light. To calculate the loss percentage in particle area, we interpolated linearly between the end of last night and the start of concurrent nighttime time stamps to estimate unaffected white pixel number. The loss percentage could then be computed based on the interpolated estimation and the captured particle areas. We then correlated the excessive blue light intensity with the percentage attenuation, allowing for a corrected white pixel number at each daytime time stamp. Despite occasional dips in the curve, the implementation of this correction yielded promising results quickly and efficiently, as detailed in below sessions. More detailed steps for this method can be found in supplemental materials.

Other supplemental figures and tables

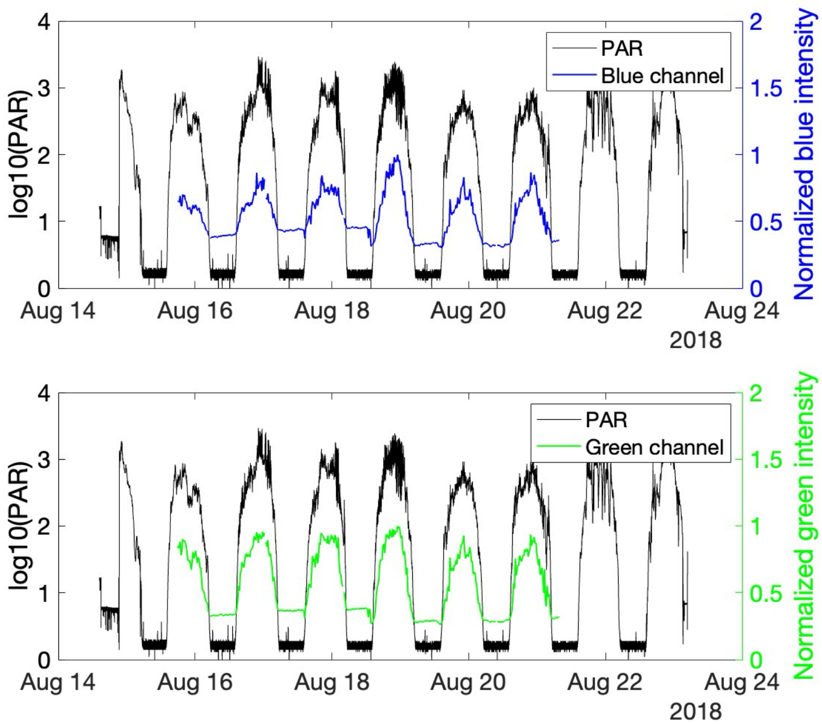

Figure S3. Time series of surface PAR and average light intensities in blue (A) and green (B) channels. The average blue/green channel light intensities were normalized by the maximum average across all image frames.

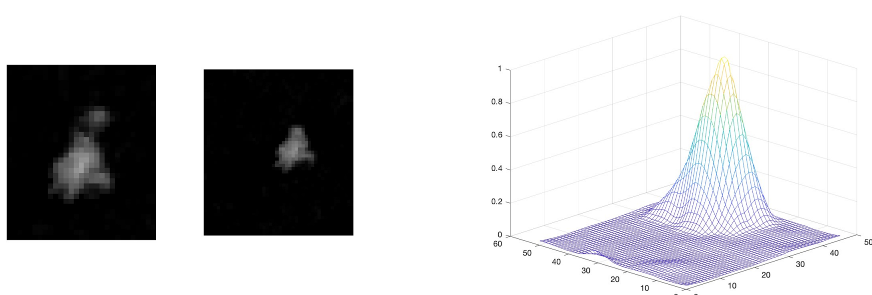

(a) (b)

Figure S4. (a) interrogation and search windows, and (b) the plane of correlation coefficients.

Table S2. Parameters that used to model the particulate carbon content of each particle type. We use the same particle types and parameters presented by Durkin et al. (2021) except dense detritus. Here *ESD* represents the equivalent spherical diameter obtained from particle projection areas, l represents the major axis length, while w is the minor axis length. Carbon mass per particle C (mg) is calculated by $C = A \cdot V^{B}$, where A is the scaling coefficient, V is the particle volume (μm^3), and B is a unitless exponent.

particle type	**shape**	**volume**	**A**	**B**
aggregates	sphere	$\frac{\pi}{6}ESD^3$	$0.1 \cdot 10^{-9}$	0.80
large loose fecal pellets	cylinder	$\frac{\pi}{4}lw^2$	$0.1 \cdot 10^{-9}$	0.83
long fecal pellets	cylinder	$\frac{\pi}{4}lw^2$	$0.1 \cdot 10^{-9}$	1
dense detritus	sphere	$\frac{\pi}{6}ESD^3$	$0.1 \cdot 10^{-9}$	0.83
salp pellets	cuboid	$\frac{1}{4}lw^2$	$0.04 \cdot 10^{-9}$	1
rhizaria	sphere	$\frac{\pi}{6}ESD^3$	$0.004 \cdot 10^{-9}$	0.939

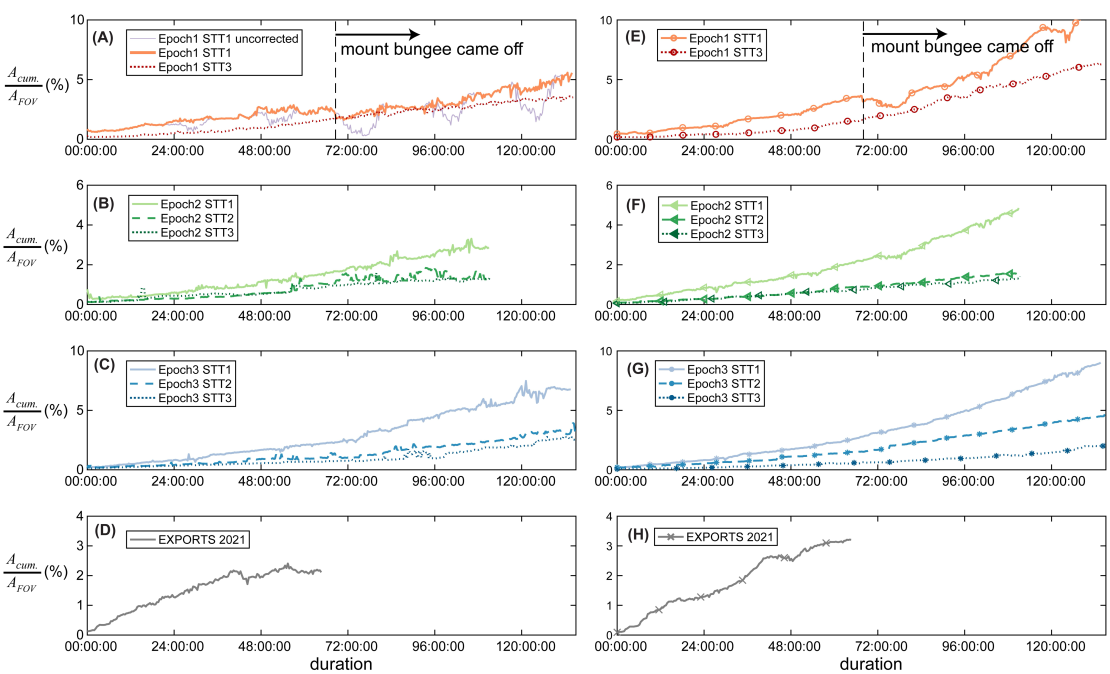

Figure S5. Accumulative fluxes at different deployments. Panels of (A), (B), (C), and (D) use the number of white pixels with the lighting correction method to quantify the time-integrated fluxes, while symbolized curves in (E), (F), (G), and (H) apply the particle classification results. Panel (A) also compares the cumulative fluxes of using the raw images or the ambient light correction in Deployment 1 STT 1. A zero duration on the x axis corresponded to the time when the deployment started. The significant discrepancy between (A) and (E) resulted from the storm during Deployment 1.

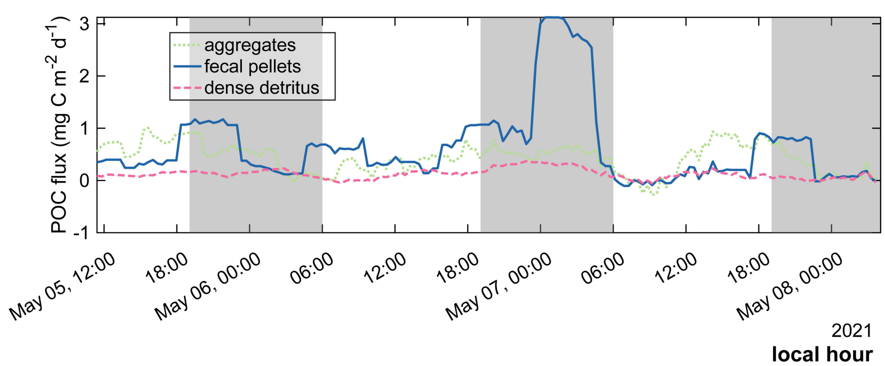

Figure S6. Time-varying POC fluxes of three particle types (aggregates in green, large loose and long fecal pellets in blue, dense detritus) in EXPORTS-NA. Shaded areas represent the nighttime.

Table S3. Coefficients of determination R^2 of different particle types across depths, with p-values in the bracket.

aggregates	STT 1	STT 2	STT 3
STT 1	1 (0)	0.91 (< 0.01)	0.84 (< 0.01)
STT 2	0.92 (< 0.01)	1 (0)	0.85 (< 0.01)
STT 3	0.85 (< 0.01)	0.84 (< 0.01)	1 (0)
large loose fecal pellets	STT 1	STT 2	STT 3
STT 1	1 (0)	0.31 (< 0.01)	0.03 (< 0.01)
STT 2	0.31 (< 0.01)	1 (0)	0.003 (0.28)

STT 3	0.03 (< 0.01)	0.003 (0.27)	1 (0)
long fecal pellets	STT 1	STT 2	STT 3
STT 1	1 (0)	0.26 (< 0.01)	0.13 (< 0.01)
STT 2	0.26 (< 0.01)	1 (0)	0.002 (0.33)
STT 3	0.17 (< 0.01)	0.002 (0.35)	1 (0)
dense detritus	STT 1	STT 2	STT 3
STT 1	1 (0)	0.005 (0.17)	0.07 (< 0.01)
STT 2	0.005 (0.17)	1 (0)	0.55 (< 0.01)
STT 3	0.06 (< 0.01)	0.55 (< 0.01)	1 (0)

Table S4. Coefficients of determination R^2 across particle types at the same depths, with p-values in the bracket.

STT 1	aggregates	large loose fecal pellets	long fecal pellets	dense detritus
aggregates	1 (0)	0.59 (< 0.01)	0.50 (< 0.01)	0.005 (0.16)
large loose fecal pellets	0.59 (< 0.01)	1 (0)	0.39 (< 0.01)	0.08 (< 0.01)
long fecal pellets	0.50 (< 0.01)	0.39 (< 0.01)	1 (0)	0.22 (< 0.01)
dense detritus	0.005 (0.16)	0.09 (< 0.01)	0.22 (< 0.01)	1 (0)
STT 2	aggregates	large loose fecal pellets	long fecal pellets	dense detritus
aggregates	1 (0)	0.09 (< 0.01)	0.14 (< 0.01)	0.85 (< 0.01)
large loose fecal pellets	0.09 (< 0.01)	1 (0)	0.39 (< 0.01)	0.09 (< 0.01)
long fecal pellets	0.14 (< 0.01)	0.39 (< 0.01)	1 (0)	0.12 (< 0.01)
dense detritus	0.85 (< 0.01)	0.09 (< 0.01)	0.12 (< 0.01)	1 (0)
STT 3	aggregates	large loose fecal pellets	long fecal pellets	dense detritus
aggregates	1 (0)	0.09 (< 0.01)	0.06 (< 0.01)	0.65 (< 0.01)
large loose fecal pellets	0.09 (< 0.01)	1 (0)	0.35 (< 0.01)	0.17 (< 0.01)
long fecal pellets	0.06 (< 0.01)	0.35 (< 0.01)	1 (0)	0.17 (< 0.01)
dense detritus	0.65 (< 0.01)	0.17 (< 0.01)	0.17 (< 0.01)	1 (0)